Final Technical Report

a. Federal Agency	Department of Energy	
b. Award Number	DE-EE0008979	
c. Project Title	EXPLORING SI HETEROJUNCTION SOLAR CELL DEGRADATION: BULK AND INTERFACE PROCESSES ANALYZED BY SIMULATIONS AND EXPERIMENTS IN ORDER TO DEVELOP MITIGATION STRATEGIES	
d. Principal Investigator	Name: Gergely T. Zimanyi Title: Professor Email address: zimanyi@ucdavis.edu Phone number: 530-400-3936	
e. Business Contact	Name: Falicia Savala Title: Fiscal Officer Email address: fsavala@ucdavis.edu Phone number: 530-752-6742	
f. Submission Date	Date: 10/27/2022	
g. DUNS Number	047120084	
h. Recipient Organization	University of California, Davis	
i. Project Period	**Start:** 4/1/2020	**End:** 10/31/2021
j. Reporting Period	**Start:** 4/1/2020	**End:** 10/31/2021
k. Report Term or Frequency	One Time	
l. Submitting Official Signature		

Major Goals & Objectives: The project objective is to explore the degradation of Si heterojunction solar cells. The method of inquiry will be the analysis of bulk and interface processes by simulation and experiment. The expected outcome is the development of degradation mitigation strategies.

This report does not contain personally identifiable information, or proprietary, confidential information.

Acknowledgment: This material is based upon work supported by the U.S. Department of Energy's Office of Energy Efficiency and Renewable Energy (EERE) under the Solar Energy Technologies Office Award Number DE-EE0008979.

Executive Summary

Heterojunction (HJ) Si solar cells have world record efficiencies approaching 27%, due to the excellent surface passivation by their a-Si layer that leads to low surface recombination velocity and high open circuit voltage (V_{OC}). In spite of the impressive efficiency records, HJ Si cells have not yet been widely adopted because of the perceived challenge that HJ cells may exhibit enhanced performance degradation, possibly related to the a-Si layer. Traditional c-Si modules typically exhibit about a 0.5%/yr efficiency degradation. In contrast, the degradation of fielded Si HJ modules was studied over 5-10 years, and reported degradation rates close to 1%/yr, about twice the rate of traditional cells. They attributed this to a new, internal degradation channel, the decay of V_{OC}, at a rate of about 0.5%/yr. The decay of V_{OC} suggests degradation processes possibly due to an increased recombination at the a-Si/c-Si interface, or in the a-Si layer.

To analyze the problem, we proposed the following. (1) The comprehensive exploration of Si HJ cell degradation caused by light-, temperature-, and potential-induced, hydrogen-assisted defect formation in the a-Si layer. (2) The comprehensive exploration of device loss processes at the interfaces of Si HJ stacks, and their impact on long-term device degradation.

For the theoretical analysis, we developed the SolDeg platform to simulate the dynamics of electronic defect generation. In our first thrust, we developed a proof-of-concept for SolDeg by analyzing Si-only stacks. First, femtosecond molecular dynamics simulations were performed to create a-Si/c-Si stacks, using the machine-learning-based Gaussian approximation potential. Second, we created shocked clusters by a cluster blaster. Third, the shocked clusters were analyzed to identify which of them supported electronic defects. Fourth, the distribution of energy barriers that control the generation of these electronic defects was determined. Fifth, an accelerated Monte Carlo method was developed to simulate the thermally activated time dependent defect generation across the barriers. -- Our main conclusions were as follows. (1) The degradation of a-Si/c-Si heterojunction solar cells via defect generation was controlled by a broad distribution of energy barriers. (2) We developed the SolDeg platform to track the microscopic dynamics of defect generation across this wide barrier distribution, and determined the time dependent defect density N(t) from femtoseconds to gigaseconds, over 24 orders of magnitude in time. (3) We have shown that a stretched exponential analytical form can successfully describe the defect generation N(t) over at least ten orders of magnitude in time. (4) We found that in relative terms Voc degrades at a rate of 0.2%/year over the first year, slowing with advancing time. (5) We developed the Time Correspondence Curve to calibrate and validate the accelerated testing of solar cells. We found a compellingly simple scaling relationship between accelerated and normal times t(normal) ~ t(accel)^(T(accel)/T(normal).

Second, we started to address the role of hydrogen in these stacks. However, we determined that the few available Si-H interatomic potentials do not provide sufficient accuracy for our simulation. On the other hand, density functional theory (DFT) studies do achieve the required high accuracy but are limited to moderate system sizes of a few hundreds of atoms by their high computational cost. Data driven, ``machine learned'' inter-atomic potentials have broken this impasse, and have been highly successful in describing a variety of amorphous materials in their elemental phase. Therefore, we extended the Gaussian approximation potential (GAP) for silicon by incorporating the interaction with hydrogen, thereby significantly improving the degree of realism with which amorphous silicon can be modelled. We trained this Si:H GAP with the energies, forces and stresses measured on DFT-constructed Si:H structures. We showed that our Si:H GAP enabled the simulation of hydrogenated silicon with an accuracy very close to DFT, but with computational expense and run times reduced by several orders of magnitude for large structures. We

demonstrated the capabilities of the Si:H GAP by creating models of hydrogenated liquid and amorphous silicon, and showing that their energies, forces and stresses were in excellent agreement with DFT results, and their structure as captured by bond and angle distributions, with DFT and experiments.

Third, we put this Si:H GAP to good use and modeled c-Si/a-Si:H stacks. We showed that in typical stacks the hydrogen atoms experienced a potential gradient that sloped away from the interface, making the hydrogen atoms drift away from the interface and thus leaving behind defect states at the interface. This degradation of the passivation is quite likely a key driver of the cell performance degradation. In fact, the experimental results of our project were very naturally explained by such a hydrogen drift. Finally, we discovered that the hydrogen potential gradient tracked the porosity gradient of a-Si:H, and so the hydrogen potential gradient can be reversed to slope toward the interface by reversing the porosity gradient. In such reversed-gradient stacks, the hydrogen did not drift away from the interface. This is a key actionable message of our theoretical work to manufacturers of c-Si/a-Si:H heterojunction cells: the cell degradation can be stopped by deposition protocols that make the porosity gradient of a-Si:H slope toward the interface.

The goal of the experimental part of the project was to investigate changes in passivation properties of hydrogenated amorphous silicon (a-Si:H(i)) and crystalline silicon (c-Si) interface due to motion of hydrogen at the interface because of light (0- or 1- Sun) and temperature (25 or 80 ºC) stressor conditions. For this c-Si wafers were bifacially coated with a-Si:H(i) and subjected to 4 different stressor conditions while passivation quality was monitored over time.

Results of the experimental work can be summarized as follows. (1) Degradation of passivation at a-Si:H(i)/c-Si interface under light and temperature exposure happens due to increase in defect density (chemical passivation) while charge density (field effect passivation) stays the same. (2) Light is essential for degradation and thus possible mechanism for degradation involves excess carriers. (3) Enhanced degradation of samples under light and heat versus only in light shows this increase is a thermally activated process. (4) Lastly, observed degradation is an interface and near-interface phenomenon since a-Si:H(i) bulk doesn't show significant change. This could be verified by performing dynamic secondary ion mass spectroscopy (d-SIMs) measurement to determine hydrogen profile in degraded samples.

Table of Contents

Background

Heterojunction (HJ) Si solar cells have world record efficiencies approaching 27%, due to the excellent surface passivation by their a-Si layer that leads to low surface recombination velocity and high open circuit voltage (V_{OC}). In spite of the impressive efficiency records, HJ Si cells have not yet been widely adopted because of the perceived challenge that HJ cells may exhibit enhanced performance degradation, possibly related to the a-Si layer. Traditional c-Si modules typically exhibit about a 0.5%/yr efficiency degradation, primarily via I_{sc} and the fill factor FF, typically attributed to external factors, such as moisture ingress and contacts. In contrast, the degradation of fielded Si HJ modules was studied over 5-10 years by groups at NREL [1] and AIST in Japan. [2] Both reported degradation rates close to 1%/yr, about twice the rate of traditional cells. They attributed this to a new, internal degradation channel, the decay of V_{OC}, at a rate of about 0.5%/yr. The decay of V_{OC} suggests degradation processes possibly due to an increased recombination at the a-Si/c-Si interface, or in the a-Si layer. Either way, the degradation is suspected to be caused by defects induced by mobile hydrogen. Very recently, co-PI Bertoni has studied the surface recombination velocity at the c-Si/a-Si interface in HJ stacks, and provided further evidence for such internal degradation processes, probably related to hydrogen effusion increasing the density of defect states. [3] This is consistent with hydrogen incorporation during deposition impacting the implied Voc for tunneling silicon oxides. [4] Finally, at the 2019 PVSC, the accelerated degradation of HJ cells was confirmed directly by representatives of Hanergy, and to some degree by the representative of Meyer Burger. All this points to the intense need to analyze the mechanism of performance degradation in c-Si/a-Si HJ cells with the goal of its mitigation.

The interest in solar cell performance degradation was further intensified recently by another development. The PV industry roadmap shows that among newly installed modules, the fraction of advanced Passivated Emitter/Rear Contact (PERC) modules will rapidly rise above 50% in the next 3 years. In these advanced PERC cells extra hydrogen is used for passivation. Alarmingly, at WCPEC 2018 and PVSC 2019, several talks reported that these advanced PERC cells exhibited unexpectedly large V_{OC} degradation. [5] Some talks related this degradation to the presence of excess hydrogen via a multi-stage process which seems to be closely related to processes seen in HJ cells.

To summarize, the accelerated degradation of V_{OC} in the Si HJ modules is well established but poorly understood. Also, the new V_{OC}-linked degradation of H-passivated PERC solar cells can critically impact the PV industry roadmap. Thus, analyzing and mitigating these degradation processes can be crucial to achieve the SETO goal of $0.03/kWh LCOE by 2030.

Project objectives

In our proposal, we outlined the following projects. (1) Comprehensive exploration of Si HJ cell degradation caused by light-, temperature-, and potential-induced, hydrogen-assisted defect formation in the a-Si layer. (2) Comprehensive exploration of device loss processes at the interfaces of Si HJ stacks, and their impact on long-term device degradation by focusing on (2.1) surface recombination velocity; (2.2) surface and mid-gap state density and energy; (2.3) degree of crystallinity; (2.4) hydrogen content; and (2.5) fabrication protocols.

Project results and discussion

We delivered all on our promised projects and tasks. In fact, we achieved considerably more. We analyzed the HJ cell degradation in Si-only c-Si/a-Si cells, as well as in c-Si/a-Si:H cells. We showed that it was possible to develop a platform, which we called SolDeg, that was capable of bridging from femtosecond dynamics to gigasecond dynamics. **(1)** Our results for Si-only stacks were as follows. (1.1) The degradation of a-Si/c-Si heterojunction solar cells via defect generation was controlled by a broad distribution of energy barriers. (1.2) We developed the SolDeg platform to track the microscopic dynamics of defect generation across this wide barrier distribution, and determined the time dependent defect density N(t) from femtoseconds to gigaseconds, over 24 orders of magnitude in time. (1.3) We have shown that a stretched exponential analytical form can successfully describe the defect generation N(t) over at least ten orders of magnitude in time. (1.4) We found that in relative terms Voc degrades at a rate of 0.2%/year over the first year, slowing with advancing time. (1.5) We developed the Time Correspondence Curve to calibrate and validate the accelerated testing of solar cells. We found a compellingly simple scaling relationship between accelerated and normal times t(normal) ~ t(accel)^(T(accel)/T(normal).

(2) Second, we developed a Machine Learning-based Si:H interatomic potential, the Si:H GAP, and we demonstrated that the Si:H GAP was capable of reaching DFT-level accuracy with computational times that were orders of magnitude shorter.

(3) Using this Si:H GAP, we showed that in typical stacks the hydrogen atoms experienced a potential gradient that sloped away from the interface, making the hydrogen atoms drift away from the interface and thus leaving behind defect states at the interface. This degradation of the passivation is quite likely a key driver of the cell performance degradation. In fact, the experimental results of our project were very naturally explained by such a hydrogen drift. Finally, we discovered that the hydrogen potential gradient tracked the porosity gradient of a-Si:H, and so the hydrogen potential gradient can be reversed to slope toward the interface by reversing the porosity gradient. In such reversed-gradient stacks, the hydrogen did not drift away from the interface. This is a key actionable message of our theoretical work to manufacturers of c-Si/a-Si:H heterojunction cells: the cell degradation can be stopped by deposition protocols that make the porosity gradient of a-Si:H slope toward the interface.

Results of the experimental work can be summarized as follows. (1) Degradation of passivation at a-Si:H(i)/c-Si interface under light and temperature exposure happens due to increase in defect density (chemical passivation) while charge density (field effect passivation) stays the same. (2) Light is essential for degradation and thus possible mechanism for degradation involves excess carriers. (3) Enhanced degradation of samples under light and heat versus only in light shows this increase is a thermally activated process. (4) Lastly, observed degradation is an interface and near-interface phenomenon since a-Si:H(i) bulk doesn't show significant change. This could be verified by performing dynamic secondary ion mass spectroscopy (d-SIMs) measurement to determine hydrogen profile in degraded samples.

Theory Task T: Comprehensive theoretical exploration of structural degradation of the cSi/aSi interface in HJ cells – Development of the **SolDeg** platform

Task T Summary: Comprehensive theoretical exploration of the degradation of the cSi/aSi interface caused by temperature-induced, hydrogen-related defect formation.

The theoretical project evolved as we learnt more and more about the problem in the opening phases. Once we sized up the difficulties associated with the presence of hydrogen, we decided to first carry out the subtasks T1-T3 for the simpler, silicon-only problem to provide a proof-of-concept for our method: that we are able connect degradation processes from the femtosecond timescale to the gigasecond time scale. This demonstration is described below in sections T1-T3. We named our method of describing Solar cell Degradation "SolDeg". Once we demonstrated the proof of concept for SolDeg on silicon-only cells, we turned to the inclusion of hydrogen. The biggest problem with hydrogen was the lack of a sufficiently precise Si-H interatomic potential. Therefore, we decided to develop the best Si-H potential ourselves by the best method we knew: by using Machine Learning (ML). We developed a collaboration with the inventor of the one of the most influential ML potentials, the Gaussian Approximation Potential, or GAP. With this collaboration we created the world's only Machine Learning-based Si-H GAP whose precision considerably exceeded that of all published Si-H potentials, and in fact achieved near DFT precision, while requiring a computer running times ten times shorter than DFT. The development is described in section T4. Finally, in section T5 we describe the application of this Si-H GAP for the analysis of the degradation processes in c-Si/a-Si:H stacks.

Subtask T1: Creation of atomistic model of cSi/aSi interface

"Subtask Summary: T1.1: Use LAMMPS to create the interface of an n-doped cSi wafer and the intrinsic aSi layer. T1.2: Improve LAMMPS [1] structure by Quantum Espresso, as needed. Metrics of improvement is lowered total energy of structure."

We developed 8 different methods to generate bulk aSi with melting and quenching within the LAMMPS [1] platform, using various Si-Si atomic potentials, such as Tersoff [2], Stillinger-Weber [3], and ReaxFF. We compared these methods by several metric, including the excess energy per atom, the radial pair correlation function, and the bond angle distribution function. We show one of our comparison tables in Table 1.

Structure/Method	E_{ex} (eV/atom) of entire supercell	E_{ex} (eV/atom) of int and a-Si
a-Si215	0.14	-
start	0.12	0.13 or 0.15
Method1 (ext)	0.16	0.18 or 0.20
Method2 (fin)	0.13	0.15 or 0.18
Method3 (num)	0.17	0.2 or 0.23
Method4 (new)	0.20	0.23
Method5 (terr-sma)	0.21	0.26 or 0.3
Method6 (sw-v2)	0.17	0.22 or 0.25
Method7 (sw-int2)	0.19	0.21
Method8 (terr-int)	0.23	0.26

Table 1: Comparison of structure-generating methods

Eventually, we discovered a very recent development in interatomic potentials, the Gaussian Approximation Potential, or GAP [4-6]. This potential was developed by generating a large number of atomic structures and environments by quantum DFT methods, and then developing an atomic potential that reproduces these structures without performing the full quantum DFT calculation. For this purpose, an Artificial Intelligence (AI), or Machine Learning (ML) method was developed that generated an interatomic potential that included many body terms, not just pair potentials and three-body potentials. In contrast to other existing potentials that are characterized by a few parameters, these GAP potentials can have thousands of parameters(!). **Fig. 1** shows the payoff for the heroic work to determine these thousands of parameters with AI/ML algorithms: the GAP potentials produces better results than any known atomic potential, according to 14 different figures of merit. Once we came across the GAP potential, we did all subsequent work with this potential.

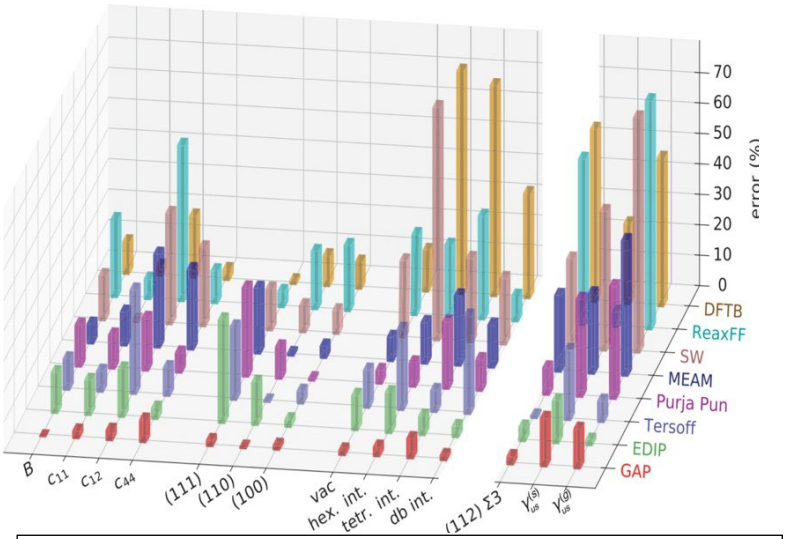

Fig. 1. Comparison of GAP with other interatomic potentials.

Further, using the GAP potential is tricky, as the positional calculation is complemented with various additional scripts. Therefore, we decided to reach out to the actual inventor of the GAP potential, prof. Csanyi of Cambridge University. With his help we mastered GAP very efficiently and achieved high reliability of our results.

Concerning project management, of course all this work is very computationally intensive. Therefore, we secured a notably large amount of computer resources. We did so by two avenues. We purchased a computer cluster of 128 nodes and housed them in the UC Davis central computational facility called FARM. Co-housing our resources with other colleagues' CPUs gave us access to their resources when they did not use them. Second, we applied for CPU time at the NERSC supercomputer center at Lawrence Berkeley lab. Our application was judged to be promising and we were given 2.5M CPU hours. All in all, we used several hundred thousand CPU hours on the UCD FARM cluster and about 1.2M CPU hours at NERSC.

In some detail, our melt-quench simulations were carried by starting with crystalline Si cubic supercells containing 216 Si atoms, with three dimensional (3D) periodic boundary conditions. The lattice constant a_0 was chosen to be 5.43 Angstrom, and the dimensions of the supercell $a=b=c=3a_0$. This lattice constant was chosen to ensure that the mass density of the resulting a-Si structures was consistent with the mass density measured by experiments.

The MD simulations were carried out using LAMMPS. The simulation time step was 1 fs. Simulations started with liquid Si at 1800K, which was cooled down to 1500K at a rate of 10^{13} K/s and equilibrated at 1500K for 100 ps. This was followed by a quench down to 500K at a rate of 10^{12} K/s. This cooling rate is consistent with previous studies. The first quench was performed in the fixed-volume and variable pressure (NVT) ensemble, while the second quench was performed

in the variable-volume and constant pressure (NPT) ensemble with fixed x and y dimensions (to match the dimensions of the cSi unit cell in the later steps), both using a Nose-Hoover thermostat and barostat. The resulting structures were then energy-minimized using a GAP-driven Hessian-free truncated Newton (HFTN) algorithm to relax all atomic positions into local minima. These energy-minimized structures were then further optimized using a DFT relaxation calculation in Quantum Espresso.

The typical excess energies (as measured relative to diamond cSi) of these structures were around 0.13-0.14 eV/atom, well within the experimentally acceptable range. The typical bond-angle distribution was 109.5 degree $\pm$11 degree, which is also consistent with typical experimental values of 108.5 degree average. The average Si-Si bond length is Å. Assuming a Si-Si bond-length cutoff of Å. Dangling (floating) bonds are missing (extra) chemical bonds of a Si atom from ideally four chemical bounds. The structures were further validated against experiment by calculating and comparing the Radial Distribution Function (RDF). The RDF, also known as the pair correlation function, measures the probability of finding the center of an atom at a given distance from the center of another atom. For aSi, the typical RDF exhibits a strong peak centered at 2.3 Å, and two weak peaks centered around 3.8 and 5.4 Å (the next-nearest and next-next-nearest neighbor distances in c-Si).

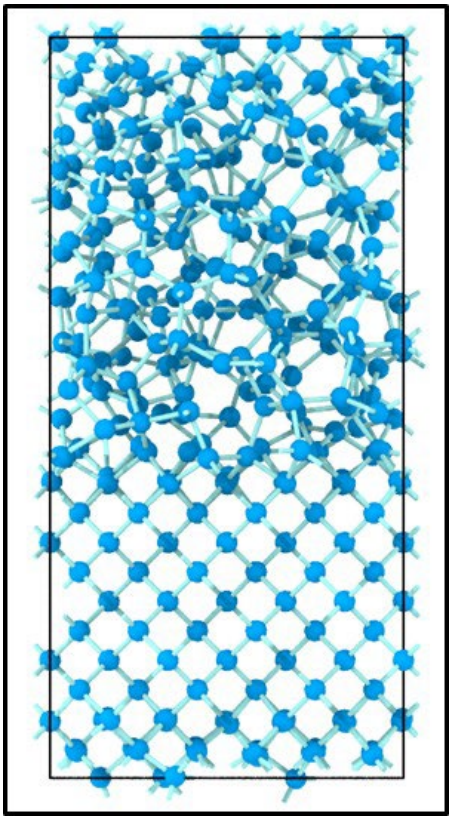

Fig. 2 shows a cSi/aSi structure created using LAMMPS with GAP.

Once we grew confident that the aSi structures we generated were really reliably good and realistic, the next task was to create cSi/aSi stacks. For this purpose, we invented different structure-generating protocols, e.g. the relative positioning of the aSi slab to the cSi slab, how to determine their optimal distance, and how to anneal the atomistic locations at the interface. The full optimization of all the cSi/aSi stack structures obtained from LAMMPS-GAP-MD were carried out at the DFT-level as implemented in the Quantum Espresso 5.2.1 software package [7],[8]. The BFGS quasi-newton algorithm, based on the trust radius procedure, was employed as the optimization algorithm for the relaxed structures.

The Perdew-Burke-Ernzerhof (PBE) exchange-correlation functional [9] was used in both the ionic relaxation and the electronic structure calculations using periodic boundary conditions. The core and valence electron interactions were described by the Norm-Conserving Pseudopotential function. Unless otherwise stated, an energy cutoff of 12Ry was employed for the plane-wave basis set and a 2×2×2 k-point mesh was used with the Monkhorst-Pack grid method for the Brillouin-zone sampling in all the calculations. A Gaussian smearing was applied to determine the band occupations and electronic density of states.

Si-heterojunction structures were created by placing the DFT-optimized aSi on top of c-Si supercells (of the same dimensions and number of atoms as the a-Si structures). Maintaining periodic boundary conditions results in structures with two aSi/cSi interfaces. At both interfaces, the aSi was placed 1.36 Å ($a_0/4$) away from the edge of the cSi supercell. This distance was chosen

by calculating the total energy of a series of structures where this distance was systematically varied, and choosing the distance which yielded the lowest total energy. These calculations were performed primarily with one representative a-Si structure, but were coarsely checked against a few others as well.

The difficulty in adopting this method of creating heterojunctions is that, while the bulk aSi layer is favorably comparable to lab-grown a-Si, the resulting cSi/aSi interfaces are highly strained and less characteristic of PCVD grown heterojunctions. Alleviating this problem requires that we go one step further, and relax each interface via thermal annealing. To avoid changing the carefully optimized aSi layers, we only annealed strips of width a_0 centered between the aSi and cSi layers at both interfaces – we have two interfaces because of the periodic boundary condition in the z/perpendicular direction. The annealing was performed at 450K for 25 ps, and was followed by cooling down to 270K at a rate of 10^{13} K/s. Both steps were performed in the NVT ensemble with a timestep of 1 fs.

Fig. 2 shows a typical cSi/aSi stack. We created about 50 such stacks. This required about 800,000 CPU hours.

Subtask T2: Analysis of defect generation

"Subtask Summary: Analyze generation and density of charged "Q" and neutral "N" defects in the structures generated in Subtask T1 as a function of hydrogen concentration and structural density. Comparative analysis of different classes of defects: charged Q defects versus neutral N defects."

We are overperforming with this task as the milestone table only called for completing this task in Q3. In order to create final states that differ only slightly from our initial states, we employ the idea of localized heating. Using LAMMPS [1] and the ML-based Silicon Gaussian Approximation Potential (GAP) [4],[5],[6], we heat our structure in a small volume containing about 5 atoms at the crystalline/amorphous interface to a temperature of 5000K while leaving the rest of the system frozen. It was found that temperatures significantly below 5000K were not efficient at generating defect states. We allow the system to evolve at this elevated temperature for 20ns in order to allow the small sub-system time to explore configuration space. After these 20ns, the sub-system is frozen very quickly, so that it cannot easily escape whatever metastable configuration it is nearest to. We then perform Conjugate Gradient minimization of the frozen structure, again using the Si GAP. This process is repeated for all of our structures at many different points on the interface in order to get a broad distribution of initial and final states.

The next task is to create configuration pairs between before heating and after heating stacks, which differ in precisely one electronic defect state. We need to identify these pairs so that we can determine the energy barrier that characterizes the creation of precisely one electronic defect. We used our 50 cSi/aSi structures and performed about 1,500 local heating procedure on them, creating what we call "defect candidate states". The heated structures differ in their atomic configurations from the initial states, and typically develop several structural defects. However, what is needed to be identified for the project are the electronic defects, not the structural defects. The product of this step is to select from the "defect candidate" stack configurations those which lead to actual electronic defects.

To determine whether an atomic structural defect induced a localized electronic state, we use the Inverse Participation Ratio (IPR) method. The localization of Kohn-Sham orbitals was computed

in details for the computer-generated a-Si/c-Si structures using the inverse participation ratio (IPR). The IPR for an eigenstate ψ_n is given as:

$$IPR_n = \frac{\Sigma_{i=1}^{I} a_{ni}^4}{(\Sigma_{i=1}^{I} a_{ni}^2)^2}$$

where a_{ni} is the coefficient of i^{th} basis set orbital in n^{th} Kohn-Sham orbital ψ_n, $(\Psi_n = \Sigma_{i=1}^{I} a_{ni}\phi_i)$ and I is the total number of basis set orbitals used in DFT calculations. The higher IPR stands for the higher degree of localization. The IPR for a completely extended state (extended equally on all the atoms) is close to zero and for a completely localized state (located on only one atom) is one.

Fig. 3 shows the calculated IPR of all the Kohn-Sham orbitals obtained from DFT versus their energy for a typical a-Si/c-Si. In agreement with our previous discussion, it is clear that the localization of the orbitals inside the mobility gap is much higher than that of its outside. The mobility gap is assigned from 5.5 to 7 eV based on the observed relatively sharp transition between localized and extended states identifying the valence/ conduction mobility edge.

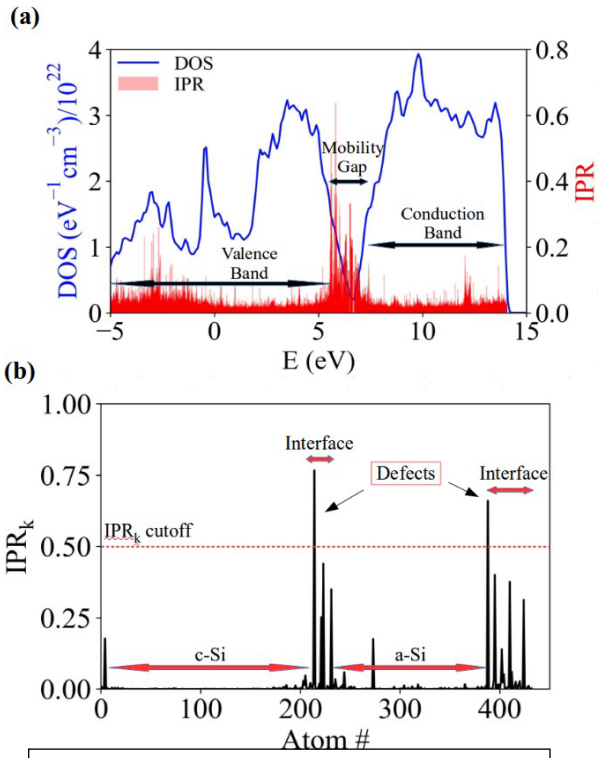

Fig. 3: (a) IPR, and (b) IPRk for a typical cSi/aSi stack

In order to define localized structural defects, we rearrange the above expression as follows:

$$IPR(\Psi_n) = \frac{\Sigma_{k=1}^{K}\Sigma_{j=1}^{J} a_{nkj}^4}{(\Sigma_{k=1}^{K}\Sigma_{j=1}^{J} a_{nkj}^2)^2}$$

where a_{nkj} is the coefficient of j^{th} atomic orbital belonging to the k^{th} atom in the n^{th} Kohn-Sham orbital. J is the total number of atomic orbitals used in DFT calculations which belong only to the k^{th} atom in the supercell. The above two equations are basically the same and give exactly the same IPR values versus energy with the difference being that the latter enables us to calculate IPR values as a function of atoms by defining a quantity namely IPR_{nkj} as follows:

$$IPR_{nkj} = \frac{a_{nkj}^4}{(\Sigma_{k=1}^{K}\Sigma_{j=1}^{J} a_{nkj}^2)^2}$$

Here IPR_{nkj} is the contribution of the k^{th} atom through its j^{th} atomic orbital in the localization of the nth Kohn-Sham orbital. One can notice that the denominators of the same for the all IPR_{nkj} as long as n is the same. Thus, there are J numbers of IPR_{nkj} values for each Kohn-Sham orbital. If there are N Kohn-Sham orbitals, then we will have NJ number of IPR_{nkj} values for each atom present in the supercell. In order to assign only one IPR value to each atom, we determine the

maximum value of IPR_{nkj} between all the NJ possible values. We name this maximum value as IPR_k and describe it as follows:

$$IPR_k = MAX^k_{n,j}\{IPR_{nkj}\}$$

where MAX^k_{nj} means the maximum value among the list of IPR_{nkj} values when k is constant and n and j have all the possible values. **Fig. 3b** shows IPR_k values for a typical a-Si/c-Si heterostructure.

We turn now to the message of the IPR method. As seen and expected, almost all of the localized states are located at the interfaces. There are no localized states in the cSi and only one localized states in the aSi. This localized states-distribution is reasonable in terms of the presence of high degree of strain at the interface and low(no) strain in the aSi(cSi) counterpart. In order to define a defect state, we need to assign a cutoff IPR_k value. Here we assume that a defect state is a state that is localized mostly on only one atom. With this assumption, the atoms with IPR_k value greater than 0.5 are defects. Therefore, there is only one defect for each interface in **Fig. 3b.**

We used this IPR method to filter out from the 1,500 defect-candidates, which of them actually supported a localized electronic defects. Having performed the IPR method on all 1,500 defect candidate states, we found about 500 supported actual electronic defects. We will use these 500 electronic defects to determine the corresponding energy barriers and their statistics in subtask **T3**, described next.

Subtask T3: Analysis of time evolution of generated defects

"Subtask Summary: Develop theory and model for the time evolution of the charged and neutral defects of Subtask T2 by describing how the migration of hydrogen away from the cSi/aSi interface increases the density of the hydrogen-related N and Q defects at the interface. The stressors of choice will be temperature and light."

We are also ahead with this subtask, which was scheduled to be performed in Q4 only. Once the initial and final states have all been created in subtask **T2**, we employ the nudged elastic band (NEB) method [11]-[14] to determine barrier heights between initial and final states. The nudged elastic band method connects two different local energy minima with several intermediate replica states, each connected to its nearest state neighbor with a spring that is nudged perpendicular to the path through state space to allow the "band" to find a saddle point. The NEB method is a tool used for determining minimum energy paths between states in some fields, but to our knowledge, this tool is not common in the solar field, so we will describe the method in some detail here.

The NEB method uses a two-component force to determine the minimum energy path (MEP). First, it uses a spring force that connects adjacent replica states with the slight modification that component of the spring force that is perpendicular to the MEP is projected out.

$$F_i^S = [k(\mathbf{R_{i+1}} - \mathbf{R_i}) - k(\mathbf{R_i} - \mathbf{R_{i-1}})] \cdot \hat{\tau}$$

where R_i represents the position in the energy landscape of the i^{th} replica, k is the spring constant, and τ is the unit vector parallel to the MEP at replica i.

The second force used in NEB is the force on the replica due to the potential, with the component parallel to the MEP projected out, so it just acts to nudge the chain of states closer to the MEP:

$$F_i^V = -\nabla V(\mathbf{R_i}) + \nabla V(\mathbf{R_i}) \cdot \hat{\tau}\hat{\tau}$$

where V is the potential energy landscape. The advantage to the NEB method over a standard elastic band method is that artifacts involved with the band cutting corners off the MEP are not a problem for the NEB method.

Our NEB simulations were performed in LAMMPS using the Si GAP. We used 32 replicas for each simulation. In our simulations we kept the non-heated atoms fixed, e.g. only the heated atoms were allowed to move replica-by-replica. The energy stopping tolerance was 10^{-6} eV, and the force stopping tolerance was 10^{-6} eV/A. The simulation timestep was 10 fs. We used the "fire" minimization algorithm, a damped dynamics method with a variable time step [15].

Fig. 4 top panel shows the result of our NEB calculations. We have determined the energy barriers that need to be overcome to create electronic defect states.

During our work we recognized that formed defects can also unwind on comparable time scales. So, we have determined the energy barriers that control the unwinding, or annihilating of the defect states. The resulting barrier distribution is shown in Fig. 4, bottom panel. Both of these barrier distributions will be used in subtask **T3** to determine the time evolution of defect generation.

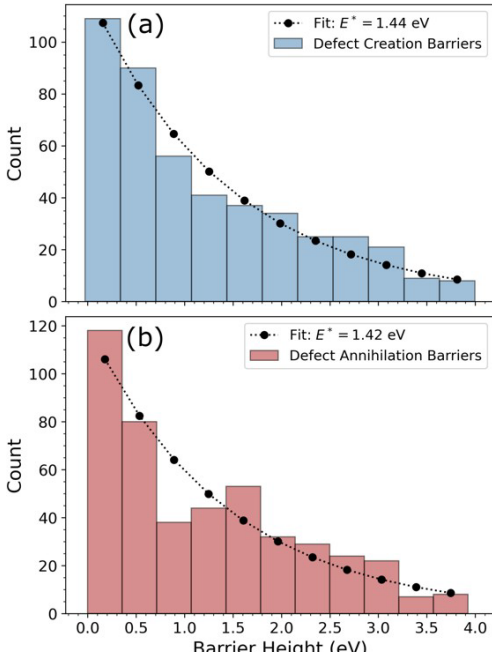

Fig. 4 Energy barrier distributions

Subtask T3: Analysis of time evolution of generated defects

Develop theory and model for the time evolution of the charged and neutral defects of Subtask T2 by describing how the migration of hydrogen away from the cSi/aSi interface increases the density of the hydrogen-related N and Q defects at the interface. The stressors of choice will be temperature and light.

In order to extract the defect density as a function of time, we turn to kinetic Monte Carlo methods. We begin by creating a large bath of potential defect sites, and randomly choosing a small percentage of them to be defected. Each site is also given an energy barrier chosen from our barrier distributions determined by the method of the previous section. Crossing a barrier of energy E corresponds to an event that changes the defect status of a site with an associated rate of:

$$\Gamma = \Gamma_0 e^{\frac{-E}{kT}}$$

where Γ_0 is the attempt frequency of the system to overcome the barrier, taken here to be 10^{-10} Hz. These rates are calculated for each site and summed to determine the total rate Γ_{tot}, and then an event is randomly selected from the possible events, with the probability of selecting event i being equal to

$$P(i) = \frac{\Gamma_i}{\Gamma_{tot}}.$$

The time is then moved forward according to

$$\Delta t = \frac{-ln(r)}{\Gamma_{tot}}$$

where r is a random number. This is equivalent to sampling a Poisson waiting time distribution. The above described method becomes computationally prohibitive when the phenomenon of interest are rare events, with rates of occurrence that are several orders of magnitude smaller than typical events. Not only are these rare events exceptionally unlikely to be chosen by the algorithm, but the number of simulation steps needed to evolve the simulation time far enough to see the rare events will be impossibly large. Using our base kinetic Monte Carlo algorithm, without any acceleration efforts, a million simulation steps only evolves the simulation time by one-hundredth of a second. This is not feasible when we are trying to observe degradation that occurs on the scales of months or years.

Our solution to this problem is to implement what is known as an accelerated super-basin kinetic Monte Carlo (AS-KMC). This method adds the extra algorithmic step of checking to see if any events which are part of a "super-basin" have been observed a set number of times, and increasing the activation energies of such events accordingly in order to lower their rate of occurrence. In the conventional terms, a super-basin consists of events which are linked to each other by high-frequency processes but are separated from the surrounding energy landscape by a low-frequency process barrier. As such, a standard kinetic Monte Carlo algorithm gets stuck in these super-basins, unable to escape, and this algorithm solves this issue by boosting them over the surrounding barrier. In our implementation, as each defect site is independent from all others, we consider each pair of defect transition rates (defect creation and defect annihilation) to be a superbasin. Leaving the superbasin in this sense means allowing the algorithm to evolve infrequently-transitioning defects. There are free parameters in the AS-KMC method that deal with how much the barriers should be raised and after how many repeated processes the barriers should be raised, but our results are largely insensitive to changes in these parameters.

The results of this AS-KMC method are shown in **Fig. 5a-b**, the vertical axis showing the defect density N(t). **Fig. 5a** illustrates the defect generation dynamics via the time dependence of the defect density N(t). Two HJ stacks were created by the SolDeg method and the time evolution of their defect densities were tracked. For one of the samples the temperature was kept at T=300K (blue) throughout, for the other, the temperature was raised to T=350K after one day (orange), in order to simulate standard accelerated testing protocols. The results of **Fig. 5a** reveal the following points.

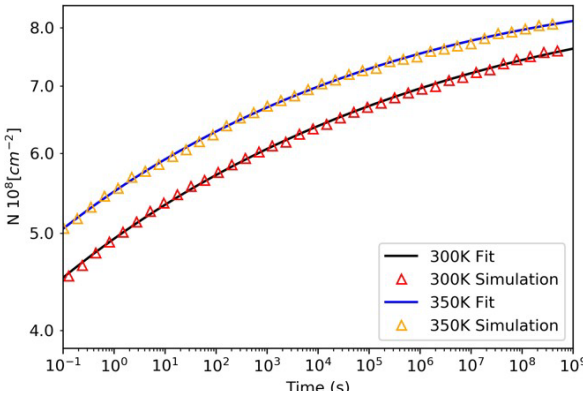

Fig. 5a Defect density N(t) as a function of time. Blue: defect generation at T=300K. Orange: generation accelerated 1 day after fabrication by elevating temperature to T=350K.

In order to develop an analytic model and understanding for these simulation results, we recall that systems that exhibit very slow dynamics are often thought of as glassy systems with a broad

distribution of energy barriers P(E). In general, the distribution of energy barriers P(E) can be translated into a distribution of "barrier crossing times" P(τ), and then coupled rate equations can be written down for defect creation and defect annihilation. The expectation value of cluster transition rates at time t can be determined by integrating over the barrier crossing time distribution P(τ) up to t which turns out to be time dependent instead of the usual constant rates, typical for well defined transition energies. This rate equation for the defect density with time dependent rates can then be solved for N(t).

The specific time dependence of N(t) depends on the functional form of the energy barrier distribution P(E). As seen in **Fig.4**, our P(E) distributions can be well-fitted with an exponential, P(E) = (1/E*) exp^(-E/E^*), with E*=1.42 eV for barrier creation and E*=1.44 eV for barrier annihilation. Following the above steps for an exponential energy barrier distribution yields a stretched exponential time dependence:

$$N(t) = N_{\text{sat}}(1 - \exp[-(t/\tau_0)^{\beta}])$$

where $\beta=k_BT/E^*$, and τ_0 is a short time cutoff. It is important to emphasize that here β was not a fitting parameter. Once we determined E* from the P(E) we computed earlier, this fixed the value of β. β being fixed makes it all the more remarkable that we were able to fit N(t,300K) over ten orders of magnitude with β(300K)=0.019= $\beta=k_B300K/E^*$, since E*=1.43 eV, the average of the defect creation and defect annihilation energy scales; and analogously, fitv N(t,350K) with β(350K)=0.022.

For completeness we note that we obtained very good fits setting τ_0 with $1/\Gamma_0$, but our fits improved by using shorter τ_0 cutoff values. Developing a physical interpretation for the best τ_0 is left for a later paper. Further, forcing power law or near-flat fits on P(E) predicted power law and logarithmic time dependencies. Such forms can achieve reasonable fits for N(t) over 2-4 orders of magnitude in time, but as the fitting range was extended, the stretched exponential fit produced the singularly best fit, and thus we conclude that the exponential for for P(E) is the natural choice.

A stretched exponential time dependence was reported for the recombination lifetime at a-Si:H/c-Si interfaces before, as well as related aging phenomena. The measurement "annealing" temperature was T=450K, and the β exponent assumed values in the 0.29-0.71 range. Accordingly, the characteristic energy scale E* of the barrier distribution that controlled this time dependence was in the range of E*=50-125 meV, an order of magnitude smaller than the Si defect energies that control the time evolution in this paper. Thus, that time dependence was probably controlled by hydrogen diffusion. Hydrogen was not considered in our model. The main messages of **Fig. 5a** are as follows.

(1) It has been customary to think about degradation processes in Si solar cells as being controlled by chemical bonds with well-defined energies, at most with a narrow distribution. But our simulations of realistic a-Si/c-Si stack interfaces show that the bond energies of a large fraction of the Si atoms, especially those close to the interface, are weakened by stretching and twisting, many to the point of being broken. Therefore, the defect generation is controlled by a broad distribution of energy barriers instead of a narrow one. One is led to the conclusion that the solar cell degradation needs to be described in terms of such wide energy barrier distributions.

(2) We developed the SolDeg platform to answer the above need. SolDeg is capable of connecting the fast atomic motions that control defect structures and play out on the femtosecond

time scale, with the slow, glassy transitions controlled by the wide distribution of energy barriers that take place over time scales up to gigaseconds, the order of 20 years. The ability of the SolDeg platform to bridge these 24 orders of magnitude in time makes it a uniquely powerful tool for a comprehensive study of defect generation in a-Si/c-Si stacks.

(3) We have shown that a simple, stretched exponential analytical form can successfully describe defect generation over an unparalleled range of ten orders of magnitude in time. This analytical form may turn out to be quite useful for the analysis of experimental degradation studies.

(4) The power of SolDeg can be further demonstrated by developing a quantitative guide to calibrate the widely used accelerated testing protocols of solar cells. **Fig. 5a** also shows the accelerated growth of the defect density in a HJ stack at the elevated temperature of T=350K. The two simulations were started with the same defect density at t=0: N(T=300K, t=0)=N(T=350K, t=0). Visibly, the T=300K and T=350K curves largely track each other: the difference is that N(T=350K, t) reaches the same defect densities as N(T=300K, t) at shorter times. This is why week-long accelerated testing can capture year-long defect generation under ambient/fielded conditions.

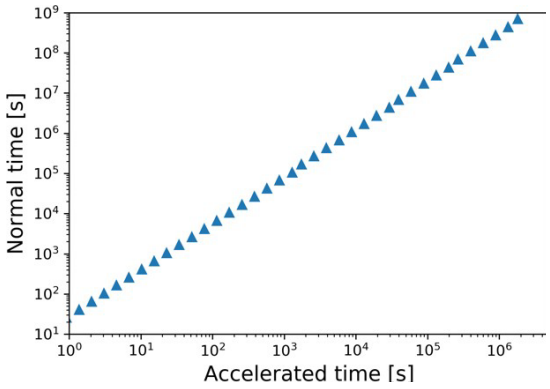

Fig. 5b. Time Correspondence Curve, translating accelerated degradation time to degradation time at standard temperature.

To turn this general observation into a quantitatively useful calibration tool, we created the Time Correspondence Curve (TCC). The TCC connects the times of accelerated testing with those times of normal, ambient degradation that produce the same defect density. In formula: TCC plots the t(accelerated) – t(normal) pairs for which N(T=350K,t(accelerated)) = N(T=300K,t(normal)). **Fig.5b** shows the resulting TCC. For example, the TCC shows that t(accelerated) =10^6 seconds of accelerated testing approximately generates the same density of defects as t(normal) =10^8 seconds or normal degradation. In general, the TCC was created by taking horizontal slices across the two curves of Fig.5a to find the corresponding pairs of times that generated the same defect density.

Even a cursory observation reveals that the TCC grows linearly on the log-log plot, i.e. as a power law over an extended, experimentally relevant time period:

$$t(\text{accelerated}) \sim t(\text{normal})^{\nu}$$

where ν =0.85, an unexpected scaling relation with an unexpected precision. Just like in **Fig. 5a**, this scaling relation is observed over the most remarkable ten orders of magnitude in time. Establishing such simple and practical correspondence relations can be a very helpful product of the SolDeg platform that can be widely used for calibrating accelerated testing protocols. Remarkably, the above-developed description in terms of an exponential P(E) that led to an stretched exponential N(t) that explained the results over ten orders of magnitude, also gives a straightforward explanation for this scaling relation. Direct manipulation of the stretched exponential formula establishes the correspondence $N(T=350K,t(\text{normal})^{300/350}) = N(T=300K, t(\text{normal})$, i.e. the stretched exponential form not only explains the existence of the scaling form of TCC, but makes a prediction for ν:

$$\nu = T(\text{normal})/T(\text{accelerated}) = 300/350 = 0.85,$$

which is exactly the exponent what the direct analysis of the TCC determined. These considerations provide a remarkably self-consistent and powerful tool set to analyze degradation processes.

Our results for Si-only stacks were as follows. (1) The degradation of a-Si/c-Si heterojunction solar cells via defect generation was controlled by a broad distribution of energy barriers. (2) We developed the SolDeg platform to track the microscopic dynamics of defect generation across this wide barrier distribution and determined the time dependent defect density N(t) from femtoseconds to gigaseconds, over 24 orders of magnitude in time. (3) We have shown that a stretched exponential analytical form can successfully describe the defect generation N(t) over at least ten orders of magnitude in time. (4) We found that in relative terms Voc degrades at a rate of 0.2%/year over the first year, slowing with advancing time. (5) We developed the Time Correspondence Curve to calibrate and validate the accelerated testing of solar cells. We found a compellingly simple scaling relationship between accelerated and normal times t(normal) ~ t(accel)^(T(accel)/T(normal). We have completed a paper that summarizes the work described so far. The paper has been submitted to and published in ACS Applied Materials and Interfaces, a top journal with an impact factor of 9.

Subtask T1-T3: Development of the Si:H interatomic potential with Machine Learning

As discussed above, next we started to address the role of hydrogen in these stacks. However, we determined that the few available Si-H interatomic potentials do not provide sufficient accuracy for our simulation. On the other hand, density functional theory (DFT) studies do achieve the required high accuracy but are limited to moderate system sizes of a few hundreds of atoms by their high computational cost. Data driven, ``machine learned'' inter-atomic potentials have broken this impasse, and have been highly successful in describing a variety of amorphous materials in their elemental phase. Therefore, we extended the Gaussian approximation potential (GAP) for silicon by incorporating the interaction with hydrogen, thereby significantly improving the degree of realism with which amorphous silicon can be modelled. We trained this Si:H GAP with the energies, forces and stresses measured on DFT-constructed Si:H structures. We showed that our Si:H GAP enabled the simulation of hydrogenated silicon with an accuracy very close to DFT, but with computational expense and run times reduced by several orders of magnitude for large structures. We demonstrated the capabilities of the Si:H GAP by creating models of hydrogenated liquid and amorphous silicon, and showing that their energies, forces and stresses were in excellent agreement with DFT results, and their structure as captured by bond and angle distributions, with DFT and experiments.

The detailed description of this work is extremely involved and has many nuances. Therefore, we refer to the preprint uploaded into the arxiv and attached to this report. Here we only highlight a few illustrative graphs that capture the true extent and magnitude of our effort, followed by the precision we achieved with the Si:H GAP. We close by simulating an excessively large sample of ~4,600 atom Si:H slab, which would take prohibitively long times to simulate with DFT, but is well within the reach of the here-developed Si:H GAP, thereby demonstrating the utility of our work.

Iteration	Structure Type
1	Optimized structures (all phases)
2	Optimized structures (all phases)
3	Low T anneal of a-Si:H
4	High T anneal of liq-Si:H
5	High T anneal of liq-Si:H
6	Med T anneal (1100K) of a-Si:H
7	Heating a-Si:H from 500K to 800K at 10^{13} K/s
8	Heating a-Si:H from 800K to 1100K at 10^{13} K/s
9	Heating a-Si:H from 1100K to 1400K at 10^{13} K/s
10	Heating a-Si:H from 1100K to 1400K at 10^{13} K/s
11	Heating a-Si:H from 800K to 1400K at 10^{12} K/s
12	Added new a-Si:H structures
13	Add new a-Si:H structures
14	Added c-Si/a-Si:H interface structures
15	Added c-Si/a-Si:H interface structures
16	Added new c-Si divacancy structures
17	Added new liq-Si:H structures
18	Added new c-Si vacancy structures
19	Added new c-Si interstitial structures
20	Low T anneal of c-Si/a-Si:H interface structures
21	Optimization of c-Si/a-Si:H interface structures
22	NPT high T anneal of liq-Si:H structures
23	NVT high T anneal of liq-Si:H structures
24	Quenching liq-Si:H from 2000K to 1500K at 10^{13} K/s
25	Annealing quenched liq-Si:H structures at 1500K
26	Quenching liq-Si:H from 1500K to 1400K at 10^{12} K/s
27	Added hydrogen passivated c-Si surface (100) and c-Si surface (111) structures

Table 2. Training protocols for the Si:H GAP

Table 2 shows that we have trained our Si:H GAP in 27 rounds on 27 classes of Si structures. These structures constitute a remarkably wide array of structures and preparation protocols for all kinds of a-Si:H structures, making the scope of applicability of the Si:H GAP quite wide.

Figs. 6a-b show how the root mean square errors of the forces acting on the Si atom (**Fig. 6a**), and H atoms (**Fig. 6b**) decreased over these 27 rounds of training.

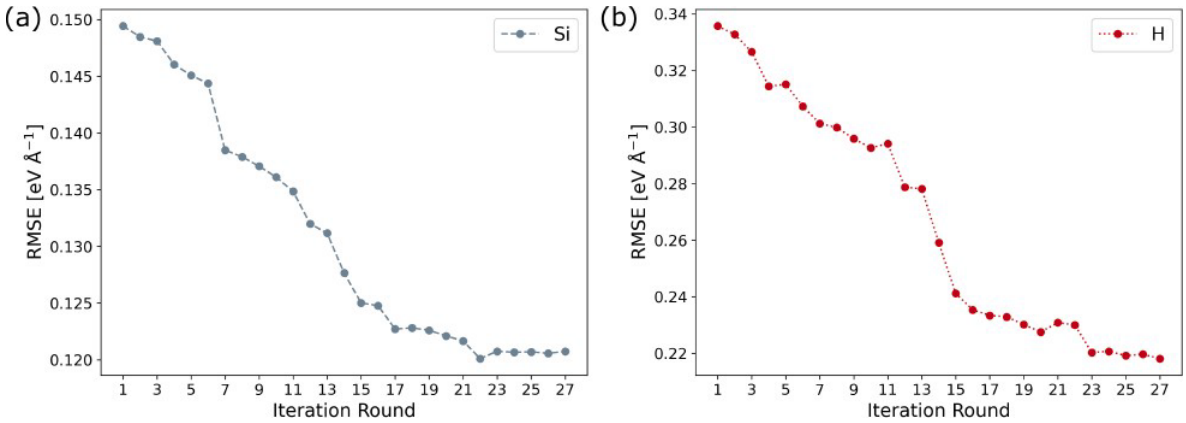

Figs. 6a-b. RMSE of atomic forces during training rounds

Fig. 7 illustrates the correspondence achieved between the energies computed by our Si:H GAP, compared to the DFT simulated energies of the very same structures. Visibly, our Si:H GAP achieved a most remarkable 4 meV/atom precision. This difference is much smaller than the energy differences expected to arise from using different DFT packages (Quantum Espresso vs. QBox vs. VASP), and thus shows that for practical purposes, our Si:H GAP achieved a precision entirely comparable to DFT precision.

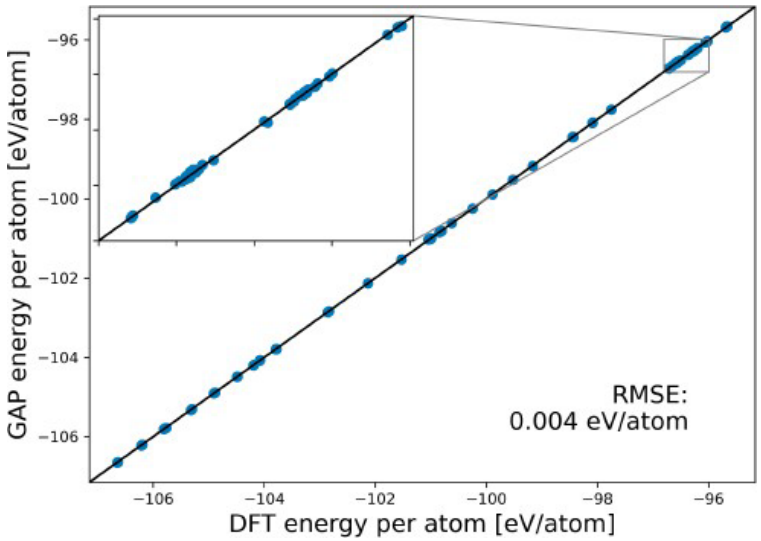

Fig. 7. RMSE of energies: Comparison of Si:H GAP and DFT

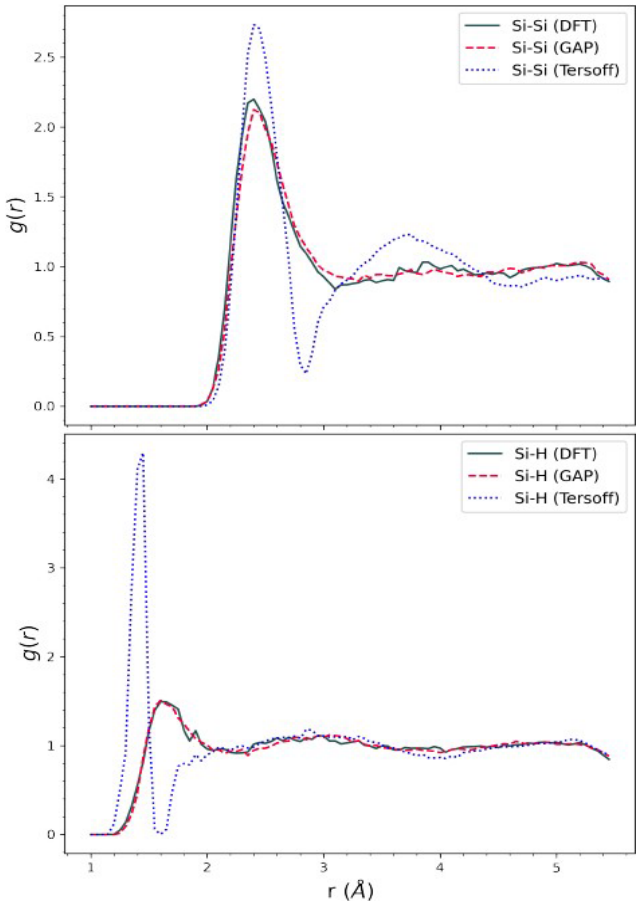

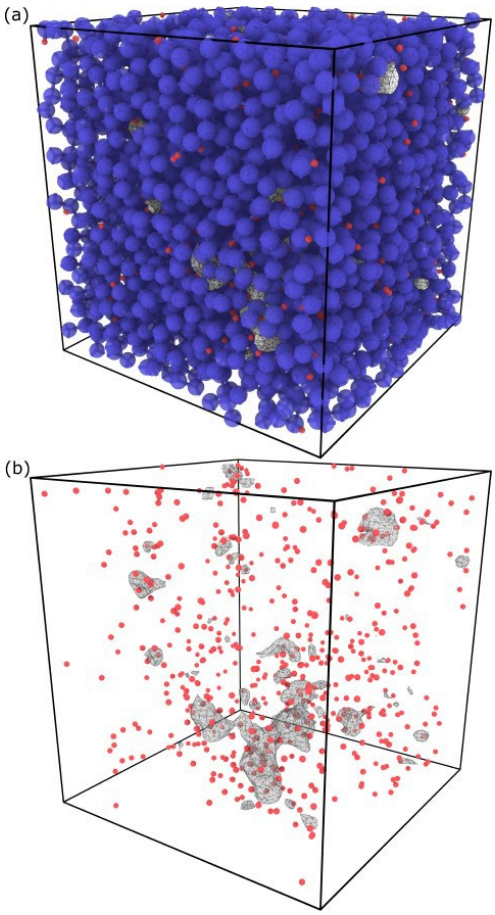

Figs. 8a-b. Si-Si and Si-H correlation functions with Si:H GAP, DFT and Tersoff.

Figs. 9a-b. a-Si:H with 4096 Si and 558 H atoms, prohibitively expensive for DFT.

Figs. 8a-b show the pair correlation functions g(r) calculated by our Si:H GAP, compared to DFT results as well as compared to the "industry-standard" Tersoff potential results. First, one notes that the Tersoff and Si:H GAP results are quite different, one might even say qualitatively different. The Si-Si pair correlation function shows a pronounced minimum around 3 Angstroms with the Tersoff potential, while DFT and Si:H GAP both predict a minimum-less, flat behavior. Further, the Si-H correlation function's major peak and subsequent behavior is again very similar for the Si:H GAP and for DFT, while it is wildly different for the Tersoff potential. These results are good indicators that there was a profound need for developing a Si:H GAP, and that the Si:H GAP we constructed indeed achieves precisions quite comparable to that of the DFT simulations.

Figs. 9a-b show the structural simulation of an a-Si:H slab with 4096 Si and 558 H atoms. Such sample sizes are prohibitively expensive to simulate with DFT, while they are quite accessible with Si:H GAP. **Fig. 9a** shows the blue Si atoms, the red H atoms and the grey voids. **Fig. 9b** omits the Si atoms. The notable formation of void structures is evident from **Figs. 9a-b**. This simulation is a constructive demonstration of the power and utility of the Si:H Gap we developed to be used by the entire Si simulation community, and specifically for the present project of c-Si/a-Si:H stack degradation. This work is to be submitted to Phys. Rev. Materials ASAP.

Subtask T1-T3: Comprehensive theoretical exploration of structural degradation of the c-Si/a-Si:H interface in HJ cells – Development of the SolDeg platform with hydrogen

As discussed, early on we made a strategic decision that the interatomic potentials available for Si-H interactions are not particularly high quality. Therefore, we decided to carry out theory tasks **T1-T3** for "silicon-only" structure. This work has been described above, completed and the corresponding paper submitted and published. Next, we developed the Si:H GAP in collaboration with prof. Gabor Csanyi of the University of Cambridge, the inventor of the machine-learning based Gaussian approximation potential, or GAP. Armed with this Si:H GAP, finally we were able to develop a comprehensive picture of c-Si/a-Si:H stacks, we performed an extensive theoretical analysis of c-Si/a-Si:H stacks. First, we created the c-Si/a-Si:H stacks. We used 12-18% hydrogen in these stacks, the experimentally relevant hydrogen concentration range. Typically, we used 216 Si atoms for the c-Si, and 216 atoms for the separately created a-Si:H slabs, the latter with 26-39 hydrogens. The a-Si:H slabs were generated by heating a crystalline Si slab to 1,800K to yield liquid Si. The liquid Si was subsequently re-solidified by cooling down to 1,500K at a rate of 10^{13} K/s before being equilibrated at 1500K for 100 ps. This solid Si was quenched further down to 500K at a rate of 10^{12} K/s, following previous studies. The first quench was performed in the constant-volume and variable-pressure (NVT) ensemble, while the second quench was performed in the variable-volume and constant-pressure (NPT) ensemble with fixed x and y cell-dimensions to match the dimensions of the c-Si unit cell in the later steps, both using a Nose-Hoover thermostat and barostat. We minimized the structural energy using a GAP-driven Hessian-free truncated Newton algorithm to relax all atomic positions into their local minima.

These relaxed a-Si:H structures were characterized with DFT, specifically making use of the Quantum Espresso 6.2.1 software package. We used the Broyden-Fletcher-Goldfarb-Shanno (BFGS) quasi-newton algorithm, based on the trust radius procedure, as the optimization algorithm. The Perdew-Burke-Ernzerhof (PBE) exchange-correlation functional was used in both the ionic relaxation and the electronic structure calculations using periodic boundary conditions. The core and valence electron interactions were described by the Norm-Conserving Pseudopotential function. Unless otherwise stated, an energy cutoff of 12 Ry was employed for the plane-wave basis set and a 2×2×2 k-point mesh was used with the Monkhorst-Pack grid method for the Brillouin-zone sampling in all the calculations. Methfessel-Paxton smearing of width 0.05 Ry was applied to determine the band occupations and electronic density of states.

Once the a-Si:H slabs were formed by LAMMPS using our Si:H GAP, and then characterized by DFT, they were merged with the c-Si slabs to form the c-Si/a-Si:H stacks. We positioned the two slabs at a distance that was determined to minimize the energy of the total stack. We explored different merging protocols. In protocol **P+,** a 6 Angstrom thick interface layer was heated to T=1,500K and then quenched. The interface layer was centered on the interface, so the first couple atomic layers of the c-Si slab were also allowed to relax. In the **P-** protocol, in contrast, we heated and the entire a-Si:H slab T=1,500K and then quenched it. We explored initial slab configurations with different amount of crystallinity.

We determined two key characteristics of the stacks, the "hydrogen potential", or "H-potential" $V_H(z)$, and the porosity. The H-potential $V_H(z)$ was computed by inserting one extra hydrogen into the a-Si:H, and then measuring the change of the energy of the stack. Typically, we inserted the extra hydrogen into 300 different locations within a stack, and then determined the H-potential at a z location by averaging its values within a 2 Angstrom wide sliding window to get good statistics. The gradient of the H-potential exerts a driving force on the hydrogen atoms that will drift

accordingly. **Figs. 10a-b** show the H-potential for stacks created by the **P+** and **P-** protocols. The red dashed lines indicate the location of the interface(s). Because of the periodic boundary condition, the a-Si that extends from z=11 A to z=29 A, interfaces with the c-Si on both sides.

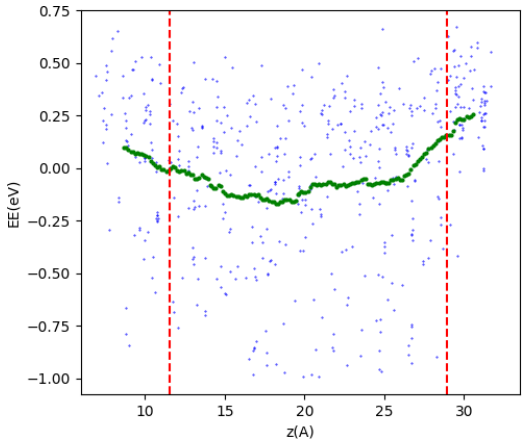

Fig. 10a. H-potential $V_H(z)$ for the **P⁻** whole-slab-quenched c-Si/a-Si:H stacks, showing a negative gradient at the interfaces at z=11A and z=29A.

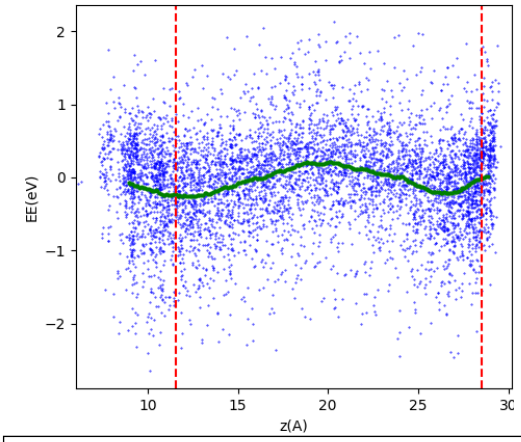

Fig. 10b. H-potential $V_H(z)$ for the **P+** interface-quenched c-Si/a-Si:H stack, showing a positive gradient at the interfaces at z=11A and z=29A.

The main message of **Fig. 10a** is that in stacks created with the **P⁻** protocol the H-potential has a negative gradient with increasing distance z from both interfaces, towards the center of the a-Si:H slab. This negative gradient drives the hydrogen atoms away from the c-Si/a-Si:H interface, towards the center of the a-Si:H slab, where $V_H(z)$ has its minimum. The hydrogen atoms that drift away from the interface leave behind dangling bonds at the interface that reduce the interface passivation and will function as recombination centers for the charge carriers in the c-Si, thereby reducing the V_{OC} of the c-Si/a-Si:H heterojunction cell. This finding is a central result of the paper: the drift of the hydrogen away from the interface is a key driver of the degradation of the open circuit voltage of heterojunction c-Si/a-Si:H cells. Having identified a key driver of the cell degradation, we will now focus on its causes and how to stop this degradation.

Fig. 1b shows that, remarkably, in stacks created with the **P**+ protocol, the gradient of the H-potential reversed its sign and became positive as the z-distance increases away from the interfaces towards the center of the a-Si:H slab. In short, in the center of the a-Si:H slabs, the H-potential has a minimum in the **P**- stacks, while a maximum in the **P**+ stacks. The robustness of this positive gradient was confirmed by simulating 30 stacks, and by inserting the extra hydrogen into close to 10,000 locations into these 30 stacks. In these **P**+ stacks, the hydrogens are not driven away from the interface since the H-potential gradient is positive. In fact, the positive gradient exerts a force on the hydrogen atoms to stay at the interface. Therefore, in **P**+ stacks the recombination rate has no reason to increase, and thus V_{OC} has no reason to decrease. This finding is a key actionable message of our work: the degradation of c-Si/a-Si:H heterojunction cells by hydrogen drift in **P**-type stacks can be stopped by changing the fabrication protocol to create **P**+ stacks.

The next task is to discover what was the mechanism that flipped the H-potential gradient in **P**+ stacks. To this end, we calculated a key microstructure characteristic: the value of the Radial Distribution Function RDF at its first peak in the lateral x-y plane: RDF1(z). RDF1(z) is calculated in a 2A thick lateral x-y slab, centered at z. RDF1(z) characterizes the porosity and microstructure of the silicon matrix, in which the hydrogen atoms drift. High RDF1(z) indicates high degree of crystalline order and thus low degree of porosity, or amorphousness. And in reverse, a low RDF1(z) indicates low degree of crystalline order, and thus high degree of porosity.

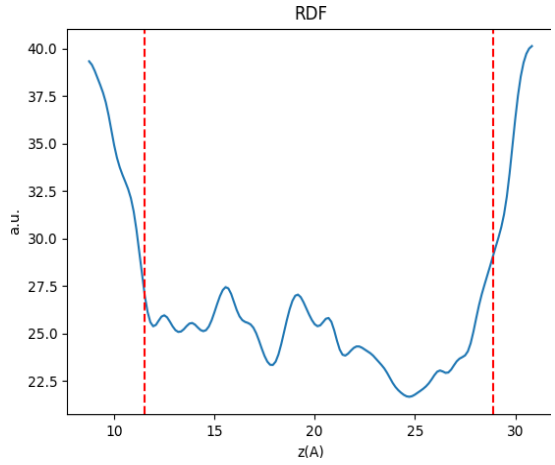

Fig. 11a. RDF1(z) for the **P**- whole-slab-quenched c-Si/a-Si:H stacks, showing a negative gradient from the interfaces at z=11A and z=29A.

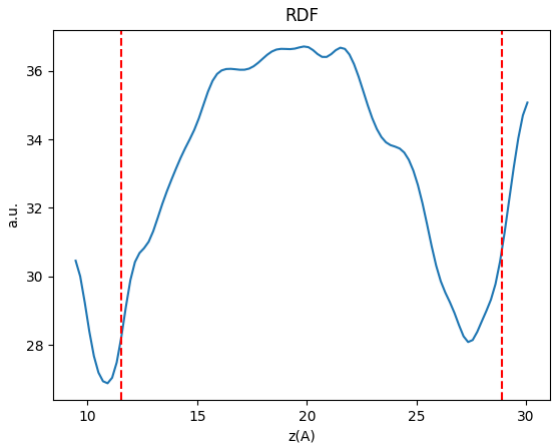

Fig. 11b. RDF1(z) for the **P**+ interface-quenched c-Si/a-Si:H stacks, showing a positive gradient from the interfaces at z=11 A and z=29A.

Fig. 11a shows that in **P**- stacks, RDF1(z) has a negative gradient with increasing distance from the interface, just like the H-potential $V_H(z)$. This correspondence with the gradient of the H-potential $V_H(z)$ provides a natural physical picture. The decrease of the first RDF peak RDF1(z) moving away from the interface indicates that the regularity of the Si atoms decreases, and thus the porosity and the disorder of the a-Si matrix increases. The porosity increasing toward the center of the a-Si slab creates an increasing amount of space for the hydrogen atoms to move between the Si atoms by crossing lower energy barriers and to find lower energy positions for themselves by drifting farther away from the interface.

Fig. 11b shows that in **P**+ stacks, in contrast, RDF1(z) flips to a positive gradient with increasing distance from the interface. This provides a natural explanation for the positive gradient for the H-potential $V_H(z)$ in **Fig. 10b**: in **P**+ stacks, RDF1(z) increases, and thus the porosity decreases away from the interface: this makes the interface more attractive and the a-Si slab center less attractive for hydrogen atoms.

To summarize, the first major result of our analysis is that in **P**- type c-Si/a-Si:H heterojunction cells the hydrogen atoms are driven away from the interface toward the a-Si slab center by a negative gradient of the H-potential $V_H(z)$, shown in **Fig. 10a**. This hydrogen drift creates new recombination centers at the interface that increases the charge carrier recombination rate and thus reduces V_{OC}, resulting in the degradation of the cell performance. This negative gradient is caused

by the negative gradient of the RDF1(z), shown in **Fig. 11a**, which indicates that the porosity of the a-Si matrix increases away from the interface, thereby making increasingly "more room" and lower energy barriers to direct the drifting hydrogen atoms toward the a-Si slab center.

Our second major result is that this degradation by hydrogen drift can be stopped by reversing the gradient of the of the H-potential by reversing the gradient of the porosity. Indeed, **Fig. 10b** showed that in **P**+ stacks, the H-potential gradient was positive, and **Fig. 11b** confirmed that this was caused by the porosity gradient changing sign relative to **P**- stacks. Thus, our simulations not only identified the likely mechanism of the cell degradation: they also articulated a technique to stop this degradation. Our simulations strongly suggest that if a c-Si/a-Si:H heterojunction cell is fabricated such that the Si matrix porosity increases towards the interface, then the driving force of the hydrogen drift is eliminated, in fact, it is reversed. This porosity gradient reversal promises to stop the degradation of the heterojunction cell by hydrogen drift. We speculate that such porosity gradients can be achieved by varying one or more deposition parameters, such as the hydrogen partial pressure, the Si-to-H mixing ratio by varying the R=H2/SiH4 ratio, or the deposition temperature as the deposition of the a-Si:H layer progresses.

For completeness, we point out that the driving force of this hydrogen-drift-degradation is not a possible gradient of the hydrogen density: it is the gradient of the silicon density. We simulated dilute stacks with 12-15% H concentration, so the effects of the hydrogen density variation, or the H-H interaction were minimal. As such, effects related, e.g., to di-hydrogen sites (di-hydrides") were not prominent in our samples. Some theories investigate the possible role of the H density variation at the c-Si/a-Si:H interface, leading to the formation of di-hydrides, followed by H drift, that is a further channel of recombination center formation at the interface. This intriguing possibility is probably additive to the physics investigated here.

Experimental Task "E": Comprehensive experimental determination of time evolution of interface parameters

The goal of the experimental part of the project was to investigate changes in passivation properties of hydrogenated amorphous silicon (a-Si:H(i)) and crystalline silicon (c-Si) interface due to motion of hydrogen at the interface because of light (0- or 1- Sun) and temperature (25 or 80 ºC) stressor conditions. For this c-Si wafers were bifacially coated with a-Si:H(i) (sample structure shown in Figure 1a) and subjected to 4 different stressor conditions (shown in Figure 1b) while passivation quality was monitored over time. Detailed description of stressor conditions and their naming is given in Table 1.

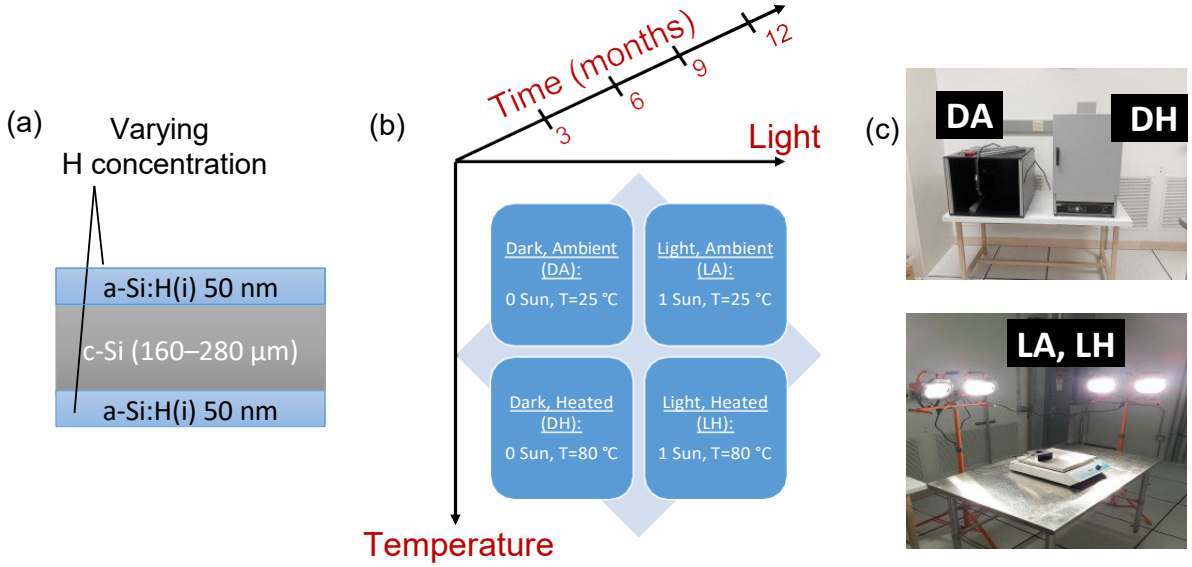

Figure 1. Structure of samples employed in this work (a), along with different stressor conditions under which they are stored (b) and lastly setup for ageing the samples is shown (c).

Table 1: Stressor Conditions

Name	Description	Number of Samples
DA	Samples stored in dark and in ambient at T=25 °C	4
DH	Samples stored in dark and heated at T=80 °C	4
LA	Samples stored under 1-Sun illumination and in ambient at T=25 °C	4
LH	Samples stored under 1-Sun illumination and heated at T=80 °C	4
	Total	16

To monitor passivation properties over time we extracted the surface recombination velocity (SRV) using the thickness variation method which required 4 samples with varying c-Si wafer thickness for each stressor condition. For 'DA' samples were aged in the dark inside a home built box, for 'DH' samples were aged in an oven maintained at 80 °C, for 'LA' samples were aged under 1 Sun illumination and finally, for 'LH' samples were placed over a hot-plate set at 80 °C in addition to 1 Sun illumination.

For LA and LH, 1 Sun illumination was generated by Halogen lamps and optical power was measured with a S350C thermal sensor from Thor Labs. Temperature was monitored constantly through thermocouples and a wireless emitter/receiver. The setup for storage and ageing is shown in Figure 1c.

Subtask E1: Creation of a set of aSi/cSi stacks with different hydrogen content

In this work a-Si:H(i) was deposited using plasma enhanced chemical vapor deposition (PECVD) technique. It is well known that by varying hydrogen to silane ratio (r=H_2/SiH_4) during deposition changes the hydrogen content (C_H) and microstructure of the a-Si:H(i). However, extreme care must be taken during hydrogen dilution as it could lead to nano-crystallization or epitaxial growth, both of which must be avoided. Therefore, we choose to investigate the properties of a-Si:H(i) deposited with 'baseline' recipe used by Solar Power Lab at Arizona State University for fabrication of their silicon heterojunction solar cells that has proven to conduce to 20% efficient heterojunctions. Exact values of different parameters in 'baseline' recipe are given in Table 2 and has r=5.

Table 2: Deposition conditions for a-Si:H(i)

Name	Value
Frequency	13.56 MHz
Pressure	3.2 Torr
Power	200 W
H_2	200 sccm
SiH_4	40 sccm
Temperature	220 °C
Deposition rate	0.5 nm/sec
Deposition time	100 seconds

We then characterized the deposited a-Si:H(i) films with Fourier transform infrared spectroscopy (FTIR) technique using Nicolet 6700 spectrometer from Thermo Electron to determine the

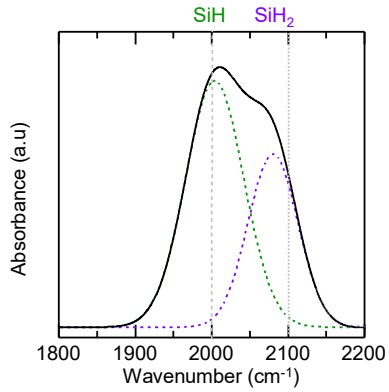

Figure 2. Measured FTIR spectra of a-Si:H(i) is shown by a solid line, whereas dotted lines are the gaussian fits to the measured curve and show the contribution of mono-and di-hydride to total absorbance.

microstructure and hydrogen content of the films. Figure 2 shows the measured FTIR spectra which has been fitted with two gaussian peaks, one centered at 2000 cm^{-1} and other centered at 2100 cm^{-1}. The area under the peak at 2000 cm^{-1} is proportional to the absorbance due to mono-hydride (SiH) bonds and similarly, area under the peak at 2100 cm^{-1} is proportional to the absorbance from SiH_2 bonds. These are often referred to as low-stretching mode (LSM) and high-stretching mode (HSM) respectively. Thus, the density of hydrogen in each mode SiH_x is proportional to the integrated area under the corresponding peak and is given by: $N_x=P_x\int\omega^{-1}\alpha(\omega)d\omega$. Here $\alpha(\omega)$ is absorption coefficient and P_x is a constant of proportionality ($P_x=P_{LSM}=P_{HSM}=9.1\times10^{19}$ cm^{-2}) [1, 2]. Finally, the atomic percentage of hydrogen in the film is obtained by dividing N_x with density of silicon atoms. Using this methodology we find the hydrogen content C_H in a-Si:H(i) to be 15 at%. Microstructure factor (R) is given by $R=A_{HSM}/[A_{HSM}+A_{LSM}]$, where A_{HSM} and A_{LSM} are areas under the HSM and LSM peak respectively. Hence, the R for baseline recipe is 0.37.

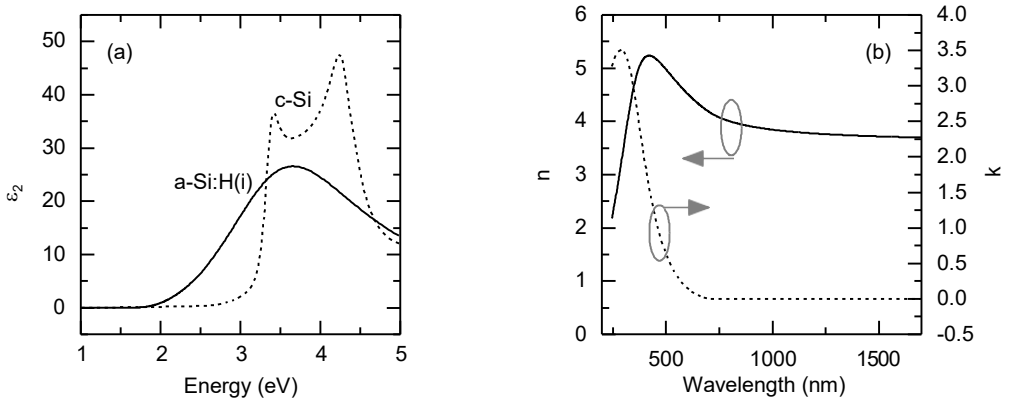

Figure 3. Complex dielectric function of a-Si:H(i) films obtained by fitting ellipsometric spectra. (a) Shown is an imaginary part of dielectric constant of a-Si:H(i) films and compared to c-Si while (b) shows the complex refractive indices.

Moreover, we also characterized a-Si:H(i) film for thickness, bandgap (E_g), refractive index and lack of crystallinity with M2000 ellipsometer from JA Woollam. Ellipsometric spectra were collected at multiple incident angles of 65, 70 and 75 degrees in reflection mode. Resulting spectra were fitted with a single Tauc-Lorentz oscillator and yielded a E_g of 1.68 eV. Moreover, the imaginary part of the determined dielectric function (ε_2) of a-Si:H(i) film shows no characteristic peaks seen in ε_2 of c-Si (shown in Figure 3a), thus ruling out presence of any nanocrystalline phase in the a-Si:H(i). Furthermore, using the value of real-part of refractive index (n) (shown in Figure 3b) we calculated the density of a-Si:H(i) ($\rho_{a\text{-}Si}$) film to be 2.25 g/cm^3 by employing the method described by Smets *et al.*, in [1].

Next, for creating a-Si:H(i)/c-Si stacks we used double-side polished, high quality float zone (FZ) *n*-type c-Si wafers with resistivity of 2.5 Ωcm and crystalline orientation of (100) with initial thickness of ~275 µm. Prior to a-Si:H(i) deposition, c-Si surfaces were thoroughly cleaned by dipping wafers in Piranha (H_2SO_4:H_2O_2|4:1) and RCA-b (H_2O:HCl:H_2O_2|6:1:1) solutions. For reducing the thickness of wafers they were etched in an HNA (HF:HNO_3:CH_3COOH|10:73:17) mixture for varying amount of time, followed by oxide removal in buffered oxide (HF:H_2O|10:1) and rinse in deionized water. Lastly, 50 nm of a-Si:H(i) was deposited on both sides of cleaned c-Si wafers using 'baseline' recipe with PECVD in Octopus I tool from INDEOtec SA.

Then to keep track of interface passivation properties effective minority carrier lifetime (τ_{eff}) measurements at temperatures between 30–230 ºC and at injection levels (Δn) between 1×10^{14}–1×10^{16} cm^{-3} were performed using WCT-120TS lifetime tester from Sinton Instruments. Data was recorded as temperature decreased from high to low and the tool was set in transient mode due to high lifetime of samples. Initial τ_{eff} measurements before ageing for all samples in each stressor condition are shown in Figure 4.

All samples in all series show drop in τ_{eff} with increasing temperature. And within respective thickness series τ_{eff} shows drop in general with decreasing c-Si thickness. Such measurements were repeated every 2 weeks for all the samples.

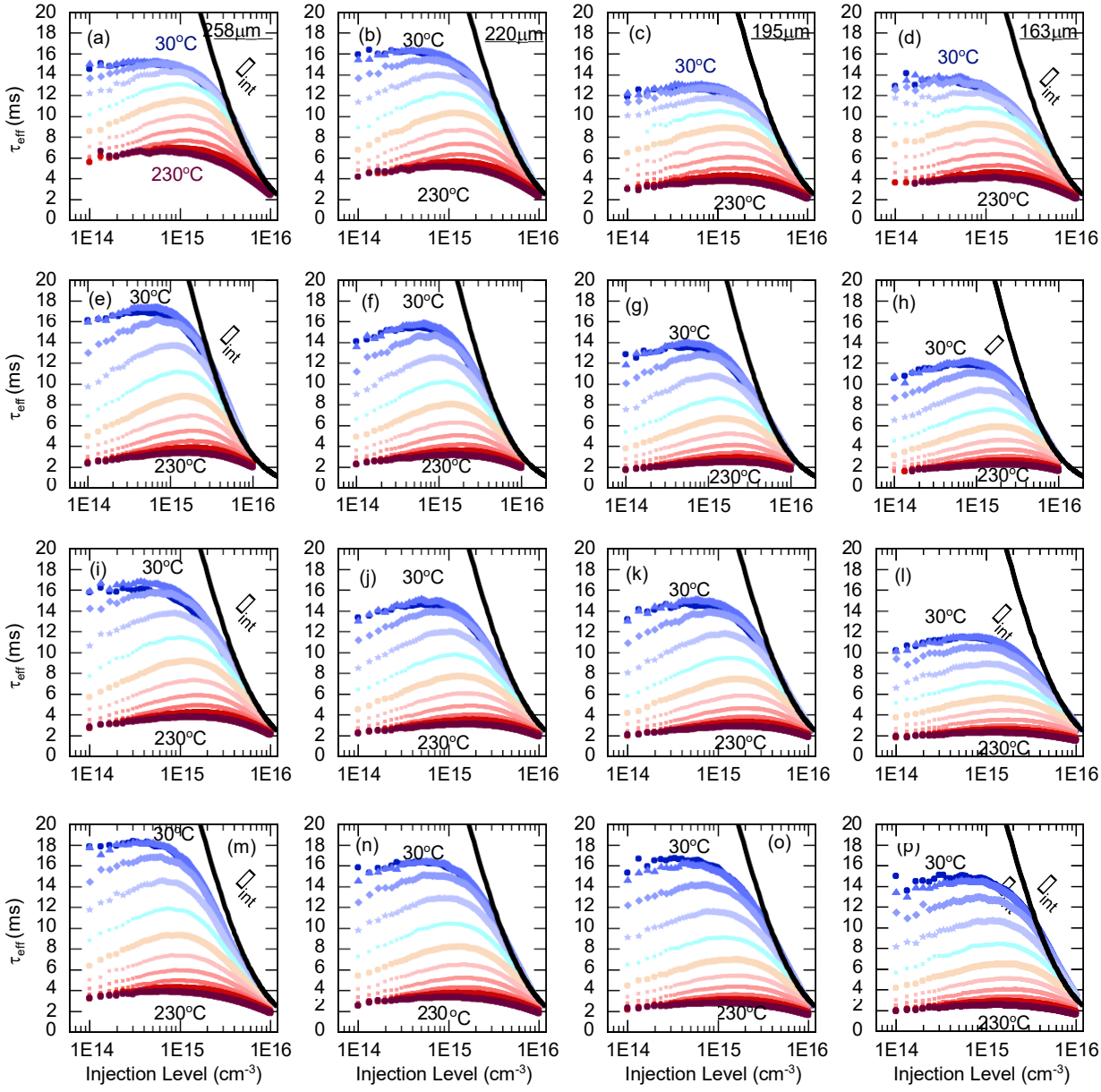

Figure 4. Shown are initial measured τ_{eff} for DA series (a-d), DH series (e-h), LA series (i-l), and LH series (m-p).

Subtask E2: Determination of interface recombination by Surface Recombination Velocity (SRV)

Effective minority carrier lifetime is a result of contributions from radiative, Auger, Shockley-Read-Hall (SRH) and surface recombination, each with its own associated lifetime, i.e., τ_{rad}, τ_{aug}, τ_{SRH} and τ_{surf} respectively. Their relationship is given by:

$$\frac{1}{\tau_{!""}} = \frac{1}{\tau_{\#\$\%}} + \frac{1}{\tau_{\$\&'}} + \frac{1}{\tau_{O*}} + \frac{1}{\tau_{+\&\#"}} \quad (1)$$

For a symmetrically passivated sample with low SRV, (1) reduces to:

$$\frac{1}{\tau_{!""}} = \&\frac{1}{\tau_{\#\$\%}} + \frac{1}{\tau_{\$\&'}} + \frac{1}{\tau_{O*}}' + \frac{2 \times SRV}{W} \quad (2)$$

where W is the thickness of the sample.

Using Equation (2) we de-convoluted the τ_{surf} and SRV from τ_{eff} measurements of a series of varying thickness a-Si:H(i)/c-Si samples under the main assumption that the bulk lifetime of c-Si (that is the addition of inverse of τ_{rad}, τ_{aug}, τ_{SRH}) remains unchanged for a given injection level and temperature. Then the $1/\tau_{eff}$ vs $1/W$ has a linear relationship and when fitted with straight line

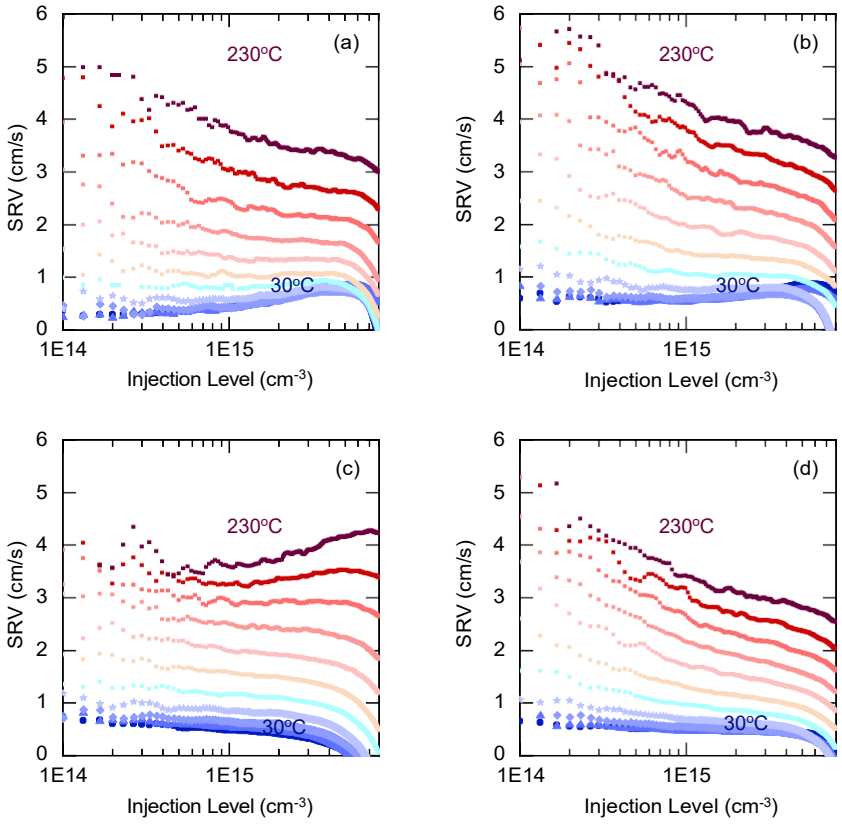

Figure 5. Shown are extracted injection-dependent SRV vs T at the start of ageing process for DA series (a), DH series (b), LA series (c) and LH series (d).

the slope of the line is equal to the twice of SRV. This process is repeated for every Δn for each T to obtain SRV(Δn, T). Figure 5 shows the extracted SRV(Δn, T) for samples in all 4 series at the start of ageing process. Results show SRV increases for increasing T which is not ideal for solar cells that operate at higher temperature in the field.

Subtask E4: Extraction of density of charged defects (Q), and neutral defects (N) at interface

Finally to obtain N_s and Q_s we fit SRV(Δn, T) (shown in Figure 5) at three distinct values of Δn (one close to V_{oc}, other close to maximum power point and last one below that) with the amphoteric defect model proposed by Olibet *et al.* [3]. In this model the inputs and their values are electron-to-hole neutral capture cross-section ratio ($\sigma^-/\sigma^- = 1/20$) and charged-to-neutral capture cross-section ratio ($\sigma'/\sigma^- = \sigma^0/\sigma^- = 500$) with $\sigma^- = 10^{012}$cm^{-2}. Figure 6a shows the SRV(Δn, T) and Figure 6b shows the corresponding SRV versus T at three injection levels along with the fits of amphoteric defect model. For this fit N_s and Q_s were allowed to vary and best-fit was obtained for N_s value of 8.3×10^7 cm^{-2} and Q_s value of -1×10^{11} cm^{-2}. A closer look reveals SRV stays fairly constant but starts to increase at T>100 ºC. Similar results have been obtained by Bernardini *et al* [4].

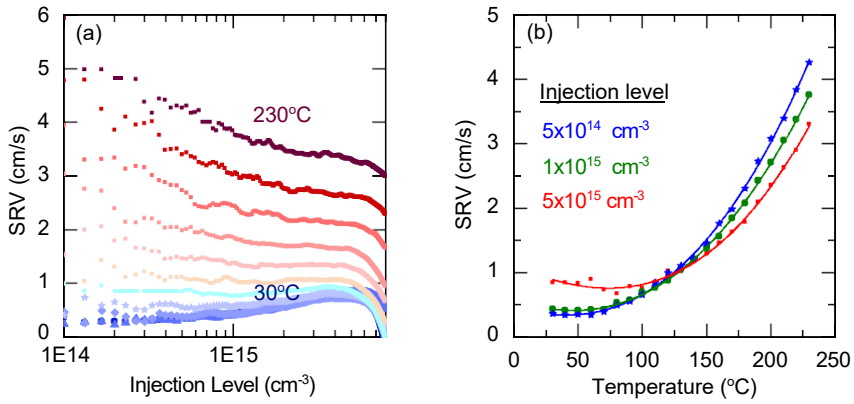

Figure 6. Shown are injection depending corresponding SRV vs T at 3 injection-levels used for fitting amphoteric defect model for DA.

In a similar manner, SRV(Δn, T) data collected every 2 weeks over a course of a year for all 4 series of samples (DA, DH, LA and LH) is fitted to extract temporal dependence of N_s and Q_s. Figure 7 shows the changes in defect and charge density for 4 sets of samples along with the changes in τ_{eff} of the thickest sample in each series. Also, shown in the left panel of Figure 7a are light induced changes in τ_{eff} reported in literature for sample structure like ours.

We found the changes in τ_{eff} over time originate due to changes in N_s while Q_s stayed the same at the value of $-(1\pm0.3)\times10^{11}$ cm^{-2} for all samples throughout the course of monitoring.

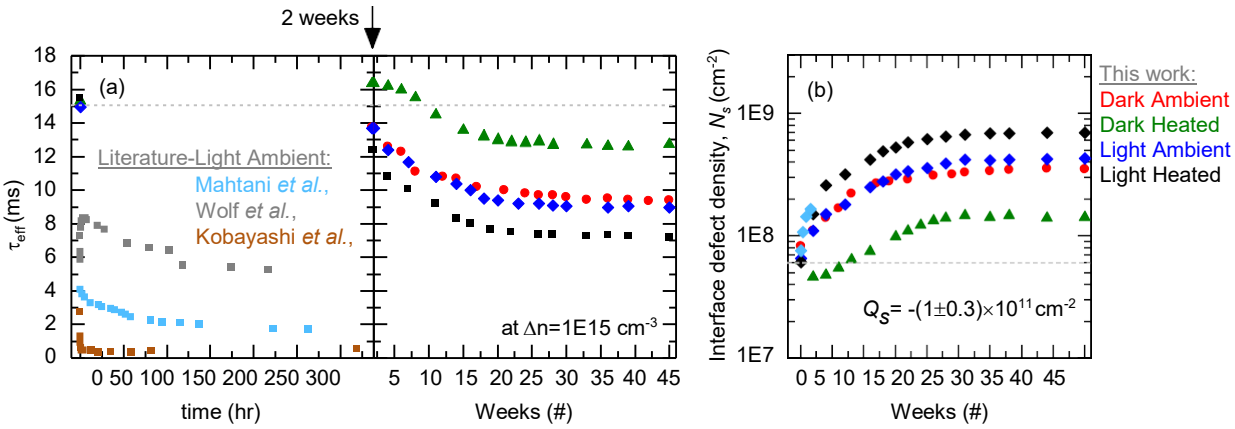

Figure 7. Shown are the change in (a) τ_{eff} and (b) N_s and Q_s over time due to different stressor conditions.

Results show the samples in the dark at 25 ºC, that is, DA, show increase in value of N_s from 8.3×10^7 cm^{-2} to a saturation value of 3.5×10^8 cm^{-2} accompanied by decrease in τ_{eff} from 15.1 ms to 9.4 ms. Degradation of passivation at a-Si:H(i)/c-Si interface in dark at ambient conditions has been reported previously but for a-Si:H(i) layers that were less than 20 nm thick [5-7]. Reasons for loss of passivation included oxidation of the a-Si:H(i) and moisture adsorption at the surface. However, a-Si:H(i) used in this work is 50 nm thick and Olibet *et al.*, has shown a-Si:H(i) films greater than 40 nm are stable in ambient condition [5]. Thus, we conclude degradation observed here is inherent to the a-Si:H(i) deposited in this work. Further evidence for this is presented later where pre- and post-ageing FTIR spectra of DA samples show no change. Thus, observed dark degradation could be caused by thermal relaxation of the a-Si:H(i) film towards equilibrium leading to rearrangement or restructuring of microstructure close to a-Si:H(i)/c-Si interface [ref]. Further support for this hypothesis comes from Holovsky *et al.*, who has shown a-Si:H(i)/c-Si stacks show increase in oxide and loss in hydrogen band in FTIR spectra only for the first 24 hours of ageing but τ_{eff} degradation continued even afterwards which led to the conclusion that a-Si:H(i) bulk and interface hydrogenation is not responsible for dark degradation in ambient conditions [7].

Degradation of LA samples that were kept at 25 ºC and subjected to 1-Sun illumination show similar time dependence and change in magnitude of N_s and τ_{eff} as DA series. Specifically, N_s increases from 6.6×10^7 cm^{-2} to a saturation value of 4.3×10^8 cm^{-2} and τ_{eff} decreased by 6.0 ms from 15.0 ms at the start of ageing process for LA samples. Similar, results for loss of passivation at a-Si:H(i)/c-Si interface under 1-Sun illumination have been observed by several other others and are shown in the left panel of Figure 7a. Also shown in Figure 7b is the change in N_s versus illumination time reported by Mahtani *et al.*, (it has been added by a constant factor to make trend in N_s values comparable to ours). Interestingly, degradation under light is a self-limiting process

which leads to saturation as observed in this work and by others. Therefore, the same saturation value of N_s and τ_{eff} for DA and LA samples is coincidental. Different mechanisms have been proposed for light-induced degradation based on non-radiative recombination of photogenerated carriers, rearrangement of microstructure at the interface and motion of hydrogen [8-12].

In contrast to all other series of samples, DH samples that were kept in the dark at 80 ºC showed the least drop in τ_{eff} and increase in N_s. Precisely, τ_{eff} increased for the first 2 weeks and correspondingly N_s decreased and after that τ_{eff} began to decrease and N_s increased gradually. Overall τ_{eff} decreased from 15.3 ms to 12.8 ms while N_s increased from 6.3×10^{7} cm^{-2} to 1.4×10^{8} cm^{-2}. Comparing DH series to DA, keeping samples at 80 ºC reduced the dark degradation observed at 25 ºC. Possible reason for this could be the dispersive diffusion of hydrogen towards the interface, released from the traps in region close to the a-Si:H(i)/c-Si interface facilitated by higher temperature of 80 ºC [9, 13, 14]. Initially, increasing τ_{eff} for the first 2 weeks and then counterbalancing the dark degradation observed for the rest of the ageing period.

Lastly, highest degradation is observed in LH samples that experienced both 1-Sun illumination and higher temperature of 80 ºC. As seen earlier, temperature of 80 ºC alone has a stabilizing effect on the a-Si:H(i)/c-Si interface, reducing dark degradation observed at 25 ºC, however, the presence of 1-Sun illumination in conjunction, results in greatest loss in τ_{eff} and increase in N_s among all the samples. Furthermore, LH and LA samples both are subjected to 1-Sun illumination, however, higher temperature of 80 ºC experienced by LH samples results in greater degradation. This suggests the observed higher loss of passivation is thermally activated. Similar increase in degradation with increase in temperature (for T<90 ºC) at constant illumination has been observed for a-Si:H films by Stutzman *et al.,* [9]. It was suggested that there is a greater probability of photoexcited carriers to recombine at sites more susceptible to photostructural changes due to increase in lifetime-mobility product at higher temperature to be the possible mechanism of increased degradation.

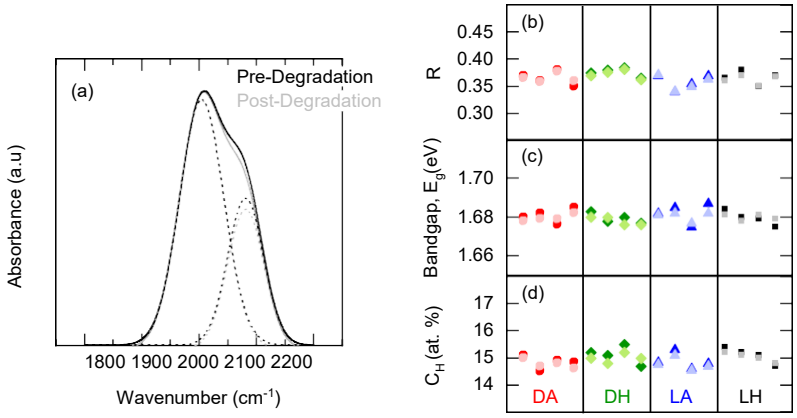

Figure 8. Comparison of FTIR spectra (a) and bandgap, microstructure factor (R) and hydrogen content (b) before (dark symbols) and after (lighter symbols) degradation.

In particular, we observe for LH samples τ_{eff} decreased by 8.3 ms from 15.5 ms at the start while N_s increased to 7.0×10^8 cm^{-2} from an initial value of 6.1×10^7 cm^{-2}. Long-term ageing results show contribution of exposure to light and heat to the degradation of a-Si:H(i)/c-Si interface passivation. Next it is important to investigate if loss of passivation at the interface under different stressor conditions also result in changes in the bulk of a-Si:H(i) in terms of microstructure, bandgap, and hydrogen content of a-Si:H(i) film. For this FTIR spectra was measured of annealed samples before the start of the ageing process and then at the end, to calculate the R and C_H and simultaneously E_g was also measured with ellipsometry. Figure 8a shows FTIR spectra pre- and post-degradation of the thickest sample in LH series which exhibits little change. Similarly, Figure 8b shows that in terms of R, C_H and E_g there is not a significant change before and after ageing in the bulk of a-Si:H(i) (within the detection limit of the FTIR tool) for all samples. This evidently shows that degradation observed in τ_{eff} under various stressor conditions is purely happening due to changes at the a-Si:H(i)/c-Si interface and near interface region. Similar evidence supporting this has been observed by Mhamdi *et al.,* who found under illumination the microstructure of a-Si:H(i)/c-Si samples didn't change even though the τ_{eff} dropped [15].

Results presented above could be summarized as follows:

1. Degradation of passivation at a-Si:H(i)/c-Si interface under light and temperature exposure happens due to increase in defect density (chemical passivation) while charge density (field effect passivation) stays the same.
2. Light is essential for degradation and thus possible mechanism for degradation involves excess carriers.
3. Enhanced degradation of samples under light and heat versus only in light shows this increase is a thermally activated process.
4. Lastly, observed degradation is an interface and near-interface phenomenon since a-Si:H(i) bulk doesn't show significant change. This could be verified by performing dynamic secondary ion mass spectroscopy (d-SIMs) measurement to determine hydrogen profile in degraded samples.

Observed degradation of lifetime in the results presented earlier showed increase in N_s over time. Possible mechanism as explained by Stutzman *et al.*, could be because of either rupturing of weak Si–Si bonds and/or breaking of Si–H bonds leading to motion of interface passivating hydrogen away from the interface into nearby region. Therefore, next we investigate if changing the environment close to the interface (microstructure of a-Si:H(i)) has an impact on the degradation. General understanding is device relevant a-Si:H(i) films have dense microstructure and offer great interface passivation quality, however in recent reports it has been shown the under-dense films can also provide similar passivation [2, 16]. But little is known about their stability. Having analysed our long-term degradation results it is clear, illumination under 1-Sun is a good test to investigate the long-term stability of interface passivation with a-Si:H(i) films having different

hydrogen content, microstructure, and bandgap. Therefore, we fabricated a-Si:H(i)/c-Si stacks by varying hydrogen-to-silane (r=H_2/SiH_4) ratio during deposition to vary the hydrogen content and

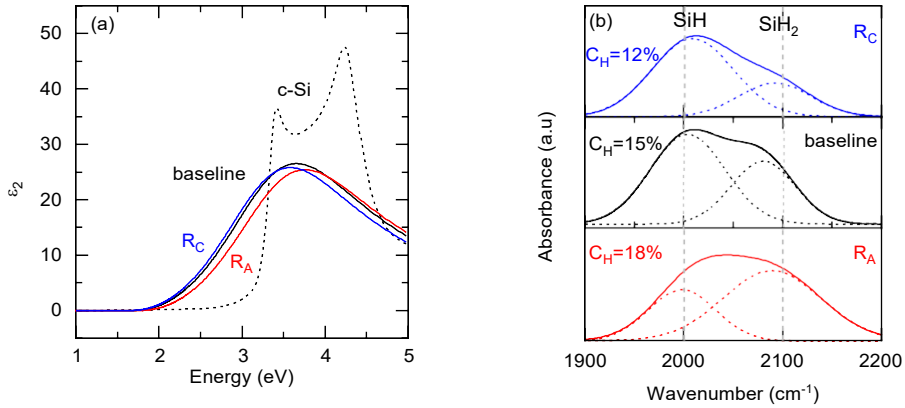

Figure 9. Optical properties of a-Si:H(i) films deposited by varying H_2/SiH_4 were analyzed. Shown are (a) dielectric function and (b) FTIR spectra of the films.

microstructure of the films. All other parameters were kept the same as baseline recipe ($R_{baseline}$) for which r was 5. Two more recipes (R_A, R_C) were used, R_A has an r of 2 and R_C has an r of 8. Figure 9 shows the optical properties of the resulting a-Si:H(i) films and compares to $R_{baseline}$. It shows by decreasing r the value of E_g increase. Thus, R_A, $R_{baseline}$ and R_C films have an E_g of 1.75, 1.68 and 1.66 eV respectively. Figure 9a further shows all films are fully amorphous, a requirement for device relevant a-Si:H(i). Figure 9b shows the FTIR spectra of the films. And it shows that decreasing r increases the SiH_2 bonding in the film which reflects the change in microstructure and density of the films. Furthermore, decreasing r leads to greater hydrogen incorporation and thus greater C_H. It is known higher hydrogen content widens the bandgap of the a-Si:H(i) which supports the results shown in Fig. 9a [17]. Several authors explored the reasons for widening of the bandgap with increasing C_H[18-20].

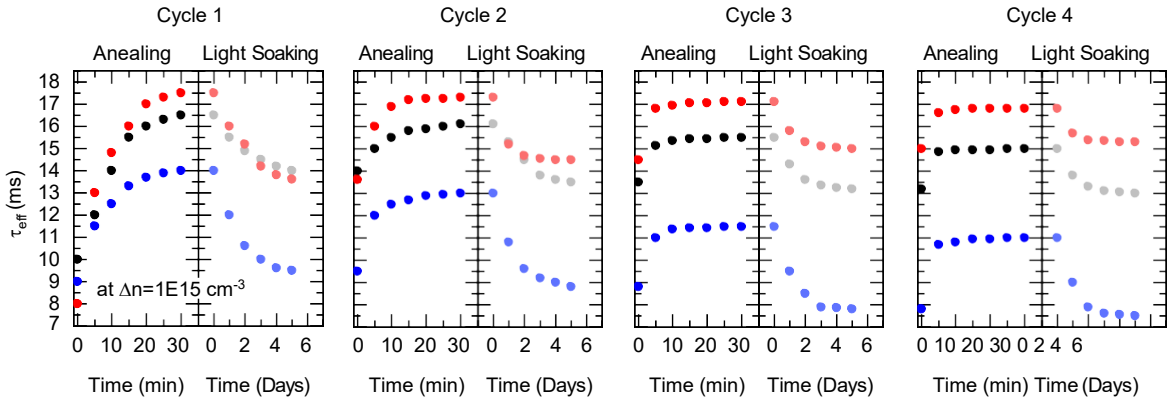

Figure 10. τ_{eff} for a-Si:H(i)/c-Si samples with different a-Si:H(i) films during LS-Ann cycles.

Next, we subjected the samples to several cycles of light soaking (LS) at 1-Sun and annealing (Ann) at 280 ºC for 30 minutes to observe the changes in τ_{eff}. The aim is to cause degradation during LS thus increasing N_s (causing the hydrogen at the interface to be free to move) and reversing the degradation during Ann stage (causing the broken bonds to be re-passivated). Figure 10 shows the results of several LS-Ann cycles. All a-Si:H(i) films show improvement in τ_{eff} during Ann stage and degradation in LS stage. Furthermore, during Ann stage the time it takes to reach the maximum attainable $\tau_{eff,max}$ becomes shorter with successive LS-Ann cycle.

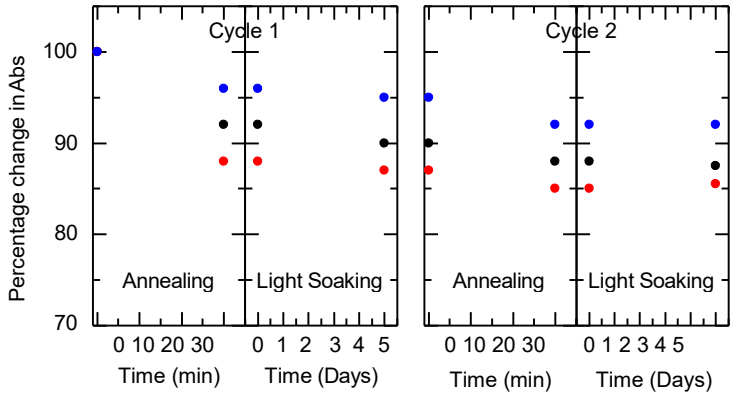

Figure 11. Shown are the changes in SiH_2 bonds with 100% at the start of Cycle 1 during LS-Ann cycles as measured from integrated area under the peak at 2100 cm^{-1} in FTIR spectra.

Moreover, we also measured the changes in microstructure during LS and Ann stages (shown in Figure 11) for the first 2 cycles (1 and 2) only since no change in microstructure was observed in subsequent cycles. We observe the decrease in SiH_2 bonds in Ann stage, however, LS stage showed no observable change. So, the latter two LS-Ann cycles (3 and 4) resemble our long-term degradation since we observed no microstructural change there as well even though τ_{eff} did continue to change. Lastly, the most important feature to observe is that lowest E_g film deposited with R_A recipe does not recover to the initial $\tau_{eff,max}$ even after annealing and so does the other two. However, the loss in $\tau_{eff,max}$ at the end of 3rd cycle to the end of 4th cycle is smallest for the highest E_g film deposited with R_C recipe and greatest for the R_A recipe deposited film that has lowest E_g. This loss could highlight the movement of hydrogen away from the interface to nearby interface region and thus is not completely reversed by annealing. This is an indication that long-term degradation is based on a mechanism that is different than Staebler Wronski Effect (SWE) based defects which are completely reversible. Similar results have been obtained Mhamdi *et al.*, but did not correlate them to the microstructure of a-Si:H(i).

These results show changing the microstructure and inevitably, also the density of the film changes the magnitude of permanent loss in $\tau_{eff,max}$. We found a-Si:H(i) with higher E_g and higher C_H (within the bandgaps and hydrogen content range investigated in this work) to be more stable. This could present a way to minimize the extent of interface passivation degradation observed over long time. However, further detailed investigation is required to quantify the reduction in degradation possible with this approach.

Significant Accomplishments and Conclusions

The main results have been described in the Executive Summary and in the Project Result sections. Here we re-summarize them for completeness.

We delivered all on our promised projects and tasks. In fact, we achieved considerably more. We analyzed the HJ cell degradation in Si-only c-Si/a-Si cells, as well as in c-Si/a-Si:H cells. We showed that it was possible to develop a platform, which we called SolDeg, that was capable of bridging from femtosecond dynamics to gigasecond dynamics. **(1)** Our results for Si-only stacks were as follows. (1.1) The degradation of a-Si/c-Si heterojunction solar cells via defect generation was controlled by a broad distribution of energy barriers. (1.2) We developed the SolDeg platform to track the microscopic dynamics of defect generation across this wide barrier distribution, and determined the time dependent defect density N(t) from femtoseconds to gigaseconds, over 24 orders of magnitude in time. (1.3) We have shown that a stretched exponential analytical form can successfully describe the defect generation N(t) over at least ten orders of magnitude in time. (1.4) We found that in relative terms Voc degrades at a rate of 0.2%/year over the first year, slowing with advancing time. (1.5) We developed the Time Correspondence Curve to calibrate and validate the accelerated testing of solar cells. We found a compellingly simple scaling relationship between accelerated and normal times t(normal) ~ t(accel)^(T(accel)/T(normal).

(2) Second, we developed a Machine Learning-based Si:H interatomic potential, the Si:H GAP, and we demonstrated that the Si:H GAP was capable of reaching DFT-level accuracy with computational times that were orders of magnitude shorter.

(3) Using this Si:H GAP, we showed that in typical stacks the hydrogen atoms experienced a potential gradient that sloped away from the interface, making the hydrogen atoms drift away from the interface and thus leaving behind defect states at the interface. This degradation of the passivation is quite likely a key driver of the cell performance degradation. In fact, the experimental results of our project were very naturally explained by such a hydrogen drift. Finally, we discovered that the hydrogen potential gradient tracked the porosity gradient of a-Si:H, and so the hydrogen potential gradient can be reversed to slope toward the interface by reversing the porosity gradient. In such reversed-gradient stacks, the hydrogen did not drift away from the interface. This is a key actionable message of our theoretical work to manufacturers of c-Si/a-Si:H heterojunction cells: the cell degradation can be stopped by deposition protocols that make the porosity gradient of a-Si:H slope toward the interface.

Results of the experimental work can be summarized as follows. (1) Degradation of passivation at a-Si:H(i)/c-Si interface under light and temperature exposure happens due to increase in defect density (chemical passivation) while charge density (field effect passivation) stays the same. (2) Light is essential for degradation and thus possible mechanism for degradation involves excess carriers. (3) Enhanced degradation of samples under light and heat versus only in light shows this increase is a thermally activated process. (4) Lastly, observed degradation is an interface and near-interface phenomenon since a-Si:H(i) bulk doesn't show significant change. This could be verified by performing dynamic secondary ion mass spectroscopy (d-SIMs) measurement to determine hydrogen profile in degraded samples.

Budget Information: Underspending of original spending plan in equipment was offset by Additional project-related spending in personnel, fringe and tuition/fee remission. Please see below.

Spending Summary by Budget Category

	Total Budget			Total Spending	
	Award -BP1	Sponsor	Cost share	Sponsor	Cost Share
a. Personnel	45242	38,600	6,643	45,200	5,309
b. Fringe Benefits	1418	733	684	185	$2,016
c. Travel					0
d & e. Equipment (indirect exempt) & Supplies	25947	25947		1,398	14250
f. Contractual	121250	97,000	24,250	84,623	24,250
g. Construction					
h. Other	15297	15297		18,941	
i. Total Direct Charges	**209,154**	**177,577**	**31,577**	**150,348**	**45,825**
j. Indirect Charges	40,846	22,423	18,423	42,304	4,175
k. Total Charges	**250,000**	**200,000**	**50,000**	**192,652**	**50,000**

Project Spend Plan

				Federal Share			Recipient Share		
Year	Quarter	From	To	Initial Plan	Actuals & Updated Plan	Cumulative	Initial Plan	Actuals & Updated Plan	Cumulative
2020	Q1	4/1/2020	6/30/2020	$60,000.00	$20,036.10	$20,036.10	$0.00	$0.00	$0.00
2020	Q2	7/1/2020	9/30/2020	$40,000.00	$94,964.42	$115,000.52	$10,000.00	$7,700.16	$7,700.16
2020	Q3	10/1/2020	12/31/2020	$40,000.00	$43,192.03	$158,192.55	$10,000.00	$0.00	$7,700.16
2020	Q4	1/1/2021	3/31/2021	$40,000.00	$33,798.39	$191,990.94	$15,000.00	$41,450.00	$49,150.16
2021	Q1	4/1/2021	6/30/2021	$20,000.00	$660.63	$192,651.57	$15,000.00	$850.01	$50,000.17
Totals				**$200,000.00**	**$192,651.57**	$192,651.57	**$50,000.00**	**$50,000.17**	$50,000.17
				Updated Federal Spend Plan total is less than the baseline.			**Updated Recipient Spend Plan total is more than the baseline.**		

Path forward: The path forward was described in detail in EERE application 2378-1753. In a short summary, we have a productive relationship with the Ballif group at EPFL. Recently, they published a study on how the degradation of the HJ cell efficiency depended on the cell architecture. The shown Figure illustrates the dependence of the HJ cell degradation on the thickness of the a-Si(i) layer and the a-Si(p) layer. For cells with an a-Si(p) layer thickness <10 nm, illumination induced defects that reduced the efficiency. This effect had a complex dependence on the thickness of the a-Si(i) layer. We will expand SolDeg to represent the a-Si(p) layer by phenomenological methods, such as by an effective field caused by bend bending and will determine the optimal (p) layer and (i) layer thicknesses to minimize defect generation.

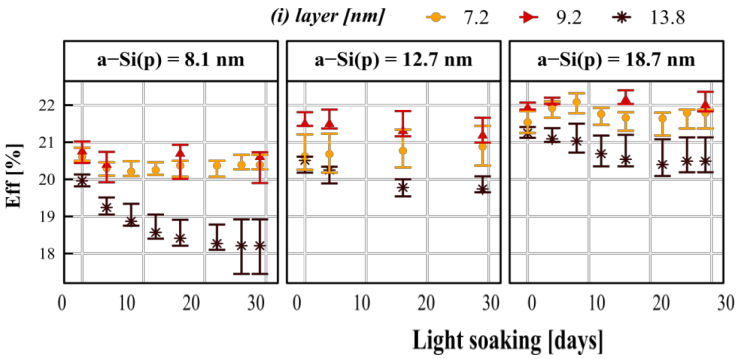

Dependence of HJ cell efficiency degradation on layer (i) layer and (p) layer thickness

Products/Publications: Three publications resulted from the project.

- The Si-only SolDeg paper was published in the ACS Applied Materials and Interfaces.
- The development of the Si:H GAP was published in Physical Review Materials.
- The c-Si/a-Si:H stack analysis, which contains a detailed and comprehensive account of the experimental work and the theoretical analysis of the H potential gradient driving hydrogen drift away from the interface has been submitted to Nature Energy.

See Accomplishments section of the RPPR-2 Template (Tab VI).

REFERENCES

[1] S. Plimpton, "Fast parallel algorithms for short-range molecular dynamics," *Journal of computational physics,* vol. 117, no. 1, pp. 1-19, 1995.

[2] J. Tersoff, "New empirical approach for the structure and energy of covalent systems," *Physical review B,* vol. 37, no. 12, p. 6991, 1988.

[3] F. H. Stillinger and T. A. Weber, "Computer simulation of local order in condensed phases of silicon," *Physical review B,* vol. 31, no. 8, p. 5262, 1985.

[4] A. P. Bartók, M. C. Payne, R. Kondor, and G. Csányi, "Gaussian approximation potentials: The accuracy of quantum mechanics, without the electrons," *Physical review letters,* vol. 104, no. 13, p. 136403, 2010.

[5] A. P. Bartók, R. Kondor, and G. Csányi, "On representing chemical environments," *Physical Review B,* vol. 87, no. 18, p. 184115, 2013.

[6] A. P. Bartók, J. Kermode, N. Bernstein, and G. Csányi, "Machine learning a general-purpose interatomic potential for silicon," *Physical Review X,* vol. 8, no. 4, p. 041048, 2018.

[7] P. Giannozzi *et al.*, "QUANTUM ESPRESSO: a modular and open-source software project for quantum simulations of materials," *Journal of physics: Condensed matter,* vol. 21, no. 39, p. 395502, 2009.

[8] P. Giannozzi *et al.*, "Advanced capabilities for materials modelling with Quantum ESPRESSO," *Journal of Physics: Condensed Matter,* vol. 29, no. 46, p. 465901, 2017.

[9] J. Perdew, K. Burke, and M. Ernzerhof, "Generalized gradient approximation made simple (vol 77, pg 3865, 1996)," *Phys. Rev. Lett,* vol. 78, pp. 1396-1396, 1992.

[10] R. V. Meidanshahi, S. Bowden, and S. M. Goodnick, "Electronic structure and localized states in amorphous Si and hydrogenated amorphous Si," *Physical Chemistry Chemical Physics,* vol. 21, no. 24, pp. 13248-13257, 2019.

[11] G. Henkelman and H. Jónsson, "Improved tangent estimate in the nudged elastic band method for finding minimum energy paths and saddle points," *The Journal of chemical physics,* vol. 113, no. 22, pp. 9978-9985, 2000.

[12] G. Henkelman, B. P. Uberuaga, and H. Jónsson, "A climbing image nudged elastic band method for finding saddle points and minimum energy paths," *The Journal of chemical physics,* vol. 113, no. 22, pp. 9901-9904, 2000.

[13] A. Nakano, "A space–time-ensemble parallel nudged elastic band algorithm formolecular kinetics simulation," *Computer Physics Communications,* vol. 178, no. 4, pp. 280-289, 2008.

[14] E. Maras, O. Trushin, A. Stukowski, T. Ala-Nissila, and H. Jonsson, "Global transition path search for dislocation formation in Ge on Si (001)," *Computer Physics Communications,* vol. 205, pp. 13-21, 2016.

[15] E. Bitzek, P. Koskinen, F. Gähler, M. Moseler, and P. Gumbsch, "Structural relaxation made simple," *Physical review letters,* vol. 97, no. 17, p. 170201, 2006.

[16] S. Olibet, E. Vallat-Sauvain, and C. Ballif, "Model for a-Si: H/c-Si interface recombination based on the amphoteric nature of silicon dangling bonds," *Physical Review B,* vol. 76, no. 3, p. 035326, 2007.

[17] S. De Wolf, S. Olibet, and C. Ballif, "Stretched-exponential a-Si: H/ c-Si interface recombination decay," *Applied Physics Letters,* vol. 93, no. 3, p. 032101, 2008.

[18] B. Wright, C. Madumelu, A. Soeriyadi, M. Wright, and B. Hallam, "Evidence for a Light-Induced Degradation Mechanism at Elevated Temperatures in Commercial N-Type Silicon Heterojunction Solar Cells," *Solar RRL,* vol. 4, no. 11, p. 2000214, 2020.

References for experimental section

[1] A. Smets, W. Kessels, and M. Van de Sanden, "Vacancies and voids in hydrogenated amorphous silicon," *Applied physics letters,* vol. 82, no. 10, pp. 1547-1549, 2003.
[2] Z. Wu *et al.*, "Role of hydrogen in modifying a-Si: H/c-Si interface passivation and band alignment for rear-emitter silicon heterojunction solar cells," *Journal of Materials Science: Materials in Electronics,* vol. 31, no. 12, pp. 9468-9474, 2020.
[3] S. Olibet, E. Vallat-Sauvain, and C. Ballif, "Model for a-Si: H/c-Si interface recombination based on the amphoteric nature of silicon dangling bonds," *Physical Review B,* vol. 76, no. 3, p. 035326, 2007.
[4] S. Bernardini and M. I. Bertoni, "Insights into the Degradation of Amorphous Silicon Passivation Layer for Heterojunction Solar Cells," *physica status solidi (a),* vol. 216, no. 4, p. 1800705, 2019.
[5] S. Olibet, E. Vallat-Sauvain, and C. Ballif, "Effect of light induced degradation on passivating properties of a-Si: H layers deposited on crystalline Si," 2006.
[6] S. Bowden, U. Das, S. Herasimenka, and R. Birkmire, "Stability of amorphous/crystalline silicon heterojunctions," in *2008 33rd IEEE Photovoltaic Specialists Conference*, 2008, pp. 1-4: IEEE.
[7] J. Holovský, S. Martín De Nicolás, S. De Wolf, and C. Ballif, "Amorphous/Crystalline Silicon Interface Stability: Correlation between Infrared Spectroscopy and Electronic Passivation Properties," *Advanced Materials Interfaces,* vol. 7, no. 20, p. 2000957, 2020.
[8] M. Stutzmann, W. Jackson, and C. Tsai, "Kinetics of the Staebler–Wronski effect in hydrogenated amorphous silicon," *Applied physics letters,* vol. 45, no. 10, pp. 1075-1077, 1984.
[9] M. Stutzmann, W. Jackson, and C. Tsai, "Light-induced metastable defects in hydrogenated amorphous silicon: A systematic study," *Physical Review B,* vol. 32, no. 1, p. 23, 1985.
[10] P. Mahtani, R. Varache, B. Jovet, C. Longeaud, J.-P. Kleider, and N. P. Kherani, "Light induced changes in the amorphous—crystalline silicon heterointerface," *Journal of Applied Physics,* vol. 114, no. 12, p. 124503, 2013.
[11] B. Clare *et al.*, "Studies of photodegradation in hydrogenated amorphous silicon," *Thin solid films,* vol. 288, no. 1-2, pp. 76-82, 1996.
[12] S. De Wolf, B. Demaurex, A. Descoeudres, and C. Ballif, "Very fast light-induced degradation of a-Si: H/c-Si (100) interfaces," *Physical Review B,* vol. 83, no. 23, p. 233301, 2011.
[13] J. Kakalios, R. Street, and n. W. Jackson, "Stretched-exponential relaxation arising from dispersive diffusion of hydrogen in amorphous silicon," *Physical review letters,* vol. 59, no. 9, p. 1037, 1987.
[14] C. G. Van de Walle, "Stretched-exponential relaxation modeled without invoking statistical distributions," *Physical Review B,* vol. 53, no. 17, p. 11292, 1996.

[15] E. M. El Mhamdi, J. Holovsky, B. Demaurex, C. Ballif, and S. De Wolf, "Is light-induced degradation of a-Si: H/c-Si interfaces reversible?," *Applied Physics Letters,* vol. 104, no. 25, p. 252108, 2014.

[16] W. Liu *et al.*, "Underdense a-Si: H film capped by a dense film as the passivation layer of a silicon heterojunction solar cell," *Journal of Applied Physics,* vol. 120, no. 17, p. 175301, 2016.

[17] M. Stuckelberger, M. Despeisse, G. Bugnon, J.-W. Schüttauf, F.-J. Haug, and C. Ballif, "Comparison of amorphous silicon absorber materials: Light-induced degradation and solar cell efficiency," *Journal of Applied Physics,* vol. 114, no. 15, p. 154509, 2013.

[18] T. Schulze, L. Korte, F. Ruske, and B. Rech, "Band lineup in amorphous/crystalline silicon heterojunctions and the impact of hydrogen microstructure and topological disorder," *Physical Review B,* vol. 83, no. 16, p. 165314, 2011.

[19] W. Liu *et al.*, "Damp-heat-stable, high-efficiency, industrial-size silicon heterojunction solar cells," *Joule,* vol. 4, no. 4, pp. 913-927, 2020.

[20] A. H. Smets *et al.*, "The relation between the bandgap and the anisotropic nature of hydrogenated amorphous silicon," *IEEE Journal of Photovoltaics,* vol. 2, no. 2, pp. 94-98, 2012.